Extreme Rainfall from Landfalling Tropical Cyclones in the Eastern United States: Hurricane Irene (2011)

MAOFENG LIU AND JAMES A. SMITH

Department of Civil and Environmental Engineering, Princeton University, Princeton, New Jersey

(Manuscript received 22 March 2016, in final form 22 August 2016)

ABSTRACT

Hurricane Irene produced catastrophic rainfall and flooding in portions of the eastern United States from 27 to 29 August 2011. Like a number of tropical cyclones that have produced extreme flooding in the northeastern United States, Hurricane Irene was undergoing extratropical transition during the period of most intense rainfall. In this study the rainfall distribution of landfalling tropical cyclones is examined, principally through analyses of radar rainfall fields and high-resolution simulations using the Weather Research and Forecasting (WRF) Model. In addition to extratropical transition, the changing storm environment at landfall and orographic precipitation mechanisms can be important players in controlling the distribution of extreme rainfall. Rainfall distribution from landfalling tropical cyclones is examined from a Lagrangian perspective, focusing on times of landfall and extratropical transition, as well as interactions of the storm circulation with mountainous terrain. WRF simulations capture important features of rainfall distribution, including the pronounced change in rainfall distribution during extratropical transition. Synoptic-scale analyses show that a deep baroclinic zone developed and strengthened in the left-front quadrant of Irene, controlling rainfall distribution over the regions experiencing most severe flooding. Numerical experiments were performed with WRF to examine the role of mountainous terrain in altering rainfall distribution. Analyses of Hurricane Irene are placed in a larger context through analyses of Hurricane Hannah (2008) and Hurricane Sandy (2012).

1. Introduction

Landfalling tropical cyclones (TCs) play an important role in determining the upper tail of flood peak distributions in the eastern United States (Smith et al. 2011; Villarini and Smith 2010; Villarini et al. 2014) and present one of the major threats to both life and property in the United States (Ashley and Ashley 2008; Barthel and Neumayer 2012). Mitigating flood risks associated with TCs remains a challenge due in part to the difficulty of characterizing the rainfall distribution from these storms after they make landfall (see, e.g., Marchok et al. 2007; Tuleya et al. 2007; Knight and Davis 2009; Konrad and Perry 2010; Kunkel et al. 2010; Barlow 2011; Brun and Barros 2014). The temporal and spatial distribution of rainfall from landfalling TCs exhibits changing structure over the storm life cycle and reflects diverse physical processes that affect the evolving storm motion, storm intensity, and storm structure (Blackwell 2000; Corbosiero and Molinari 2003; Rogers et al. 2003; Chen et al. 2006; Dong et al. 2010). Consequently, landfalling TC rainfall displays multiscale features and varies greatly over time.

Of particular importance for landfalling TC rainfall distribution are the processes associated with extratropical transition (ET), involving the interplay of tropical cyclones and baroclinic disturbances (Colle 2003; Atallah et al. 2007; Gao et al. 2009). The potential vorticity (PV) perspective (Hoskins et al. 1985) has provided a useful framework for examining hurricane–trough interactions. Hurricane Floyd (1999) exhibited a left-of-track rainfall distribution during ET in which the juxtaposition of an upper-level positive PV anomaly from the cold core trough and lower-level PV anomaly from the warm core hurricane produced a deep baroclinic zone along the U.S. East Coast (Atallah and Bosart 2003). Atallah et al. (2007) synthesized rainfall distribution from landfalling TCs over the eastern United States, with particular reference to left-of-track and right-of-track rainfall distribution (see also Bosart and Lackmann 1995; Jones et al. 2003).

Corresponding author address: Maofeng Liu, Department of Civil and Environmental Engineering, Princeton University, E208 Equad, Princeton, NJ 08544.
E-mail: maofeng@princeton.edu

DOI: 10.1175/JHM-D-16-0072.1

The influence of vertical wind shear on rainfall distribution is well documented in previous studies. Corbosiero and Molinari (2002) analyzed the azimuthal distribution of cloud-to-ground (CG) lightning in Atlantic TCs using data from National Lightning Detection Network (NLDN). It was found that most flashes occurred downshear, with a slight preference on the downshear left in the inner rainband (defined as the inner 100 km from the storm center) and a slight preference on the downshear right in the outer rainband (with radii between 100 and 300 km from the storm center). Chen et al. (2006) examined the influence of wind shear and storm motion on rainfall asymmetry of tropical cyclones in all oceanic basins using data from Tropical Rainfall Measuring Mission (TRMM) Microwave Imager (TMI) rainfall estimates. Wind shear dominated the rainfall asymmetry when shear was $>5\,\mathrm{m\,s^{-1}}$ and the asymmetry maximum was principally on the downshear left. Similar results were found through modeling studies of Hurricane Bonnie (1998) (Rogers et al. 2003). A statistical hurricane rainfall prediction model developed by Marks et al. (2002) [see Tuleya et al. (2007) for model descriptions] showed improved results after vertical wind shear was used to account for the shear-generated rainfall asymmetry (Lonfat et al. 2007).

Orographic precipitation mechanisms also contribute to extreme TC rainfall and flooding in the eastern United States, as documented for Hurricane Fran in 1996 (Sturdevant-Rees et al. 2001), Hurricane Floyd in 1999 (Colle 2003), and Hurricane Isabel in 2003 (Lin et al. 2010). Strong low-level winds from TCs promote an environment with a large Froude number. This flow combines with abundant moisture to enhance orographic rainfall production through vertical motion of moist air along the windward slopes of the mountain (Colle 2003; Gao et al. 2009; Xie and Zhang 2012). This simple lifting mechanism can be complicated, however, by microphysical and dynamical interactions of background TC rainfall with orographic effects (Yu and Cheng 2013). In recent research, topographic precipitation enhancement of TCs has been studied through both radar observations (Smith et al. 2009; Yu and Cheng 2013) and numerical simulations (Colle 2003; Huang et al. 2014).

In this study we examine rainfall distribution of landfalling tropical cyclones, principally through analyses of Hurricane Irene (2011). We present analyses of rainfall distribution based on radar rainfall fields and analyses of rainfall and storm environment using high-resolution simulations performed with the Weather Research and Forecasting (WRF) Model. Our analyses are motivated by problems of flood hazard characterization for which simplified models of tropical cyclone rainfall are needed (Marks et al. 2002; Lonfat et al. 2007; Marchok et al. 2007; Tuleya et al. 2007; Langousis and Veneziano 2009). We compare the structure and evolution of rainfall from Hurricane Irene with a tropical cyclone that had a very similar track, Hurricane Hanna (2008), and a tropical cyclone with a very different track, Hurricane Sandy (2012).

Hurricane Irene produced heavy rainfall along the U.S. East Coast, leading to extreme flooding in these areas. Irene made landfall in North Carolina and transitioned into an extratropical system through interaction with a midlatitude trough. Extreme rainfall and flooding were concentrated in mountainous terrain of the Appalachians region. Hurricane Irene was directly responsible for 49 deaths, with 41 in the United States. Half of the fatalities in the United States were attributed to rainfall-induced floods (Avila and Cangialosi 2011). Irene ranks seventh among U.S. hurricanes in terms of property damages (Blake et al. 2011). Inland flooding and storm surge were responsible for $7.2 billion (2011 USD) in economic losses, based on National Flood Insurance Program data, accounting for 45.5% of the total loss estimate (Avila and Cangialosi 2011).

Previous studies of landfalling TC rainfall focused on the spatial distribution of storm total rainfall (Rogers et al. 2003; Chen et al. 2006; Atallah et al. 2007; Milrad et al. 2009). In this study, we focus on the time evolution of the spatial structure of rainfall. We use procedures presented in Lin et al. (2010), Villarini et al. (2011), and Smith et al. (2011) to examine temporal evolution of rainfall from a Lagrangian perspective, focusing on the radial and azimuthal distribution of rainfall. Key questions addressed in this paper are the following. What are the physical processes controlling structural changes in rainfall distribution from landfalling tropical cyclones? How does extratropical transition control rainfall distribution from landfalling tropical cyclones in the eastern United States?

The paper is organized as follows. In section 2, we introduce the data used for examining rainfall distribution from landfalling tropical cyclones and the WRF Model configuration used for high-resolution simulations. Results are presented in section 3, and a summary and conclusions are given in section 4.

2. Data and methods

a. *WRF Model configuration*

The WRF Model, developed by the National Center for Atmospheric Research (NCAR), is a fully compressible, nonhydrostatic, mesoscale model. In this study, the Advanced Research version of WRF (ARW, version 3.4.1) was used. It is implemented in three one-way nested

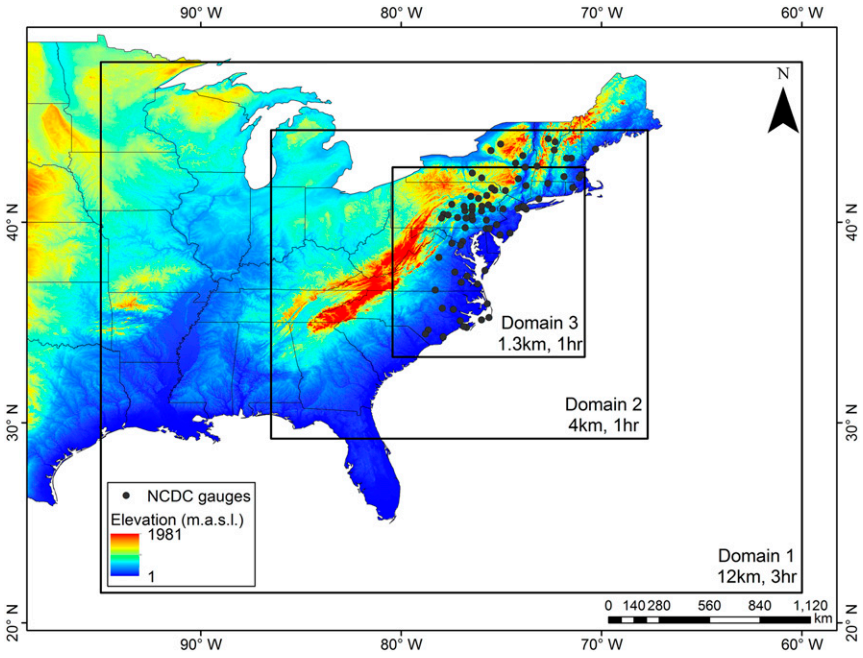

FIG. 1. WRF domain configurations used for Hurricane Irene (2011) simulation. Black circles denote locations of 77 NCDC rain gauges.

domains with horizontal grid resolutions of 12, 4, and 1.3 km, respectively (Fig. 1). As shown in Fig. 1, the outer domain (d01) covers the central and eastern United States. The intermediate domain (d02) stretches from Florida to Maine. The inner domain (d03) focuses on the region from North Carolina to New York. The x (west–east) and y (south–north) direction grid numbers are 230 × 240, 391 × 421, and 589 × 772 for the 12-, 4-, and 1.3-km domains, respectively. Unless specifically noted, analyses will be based on results from the intermediate domain (d02).

The physics parameterizations used in this study include 1) a modified Kain–Fritsch scheme for cumulus parameterization in the 12-km resolution domain and no cumulus parameterization in 4- and 1.3-km resolution domains; 2) a WRF single-moment 6-class microphysics scheme (WSM6); 3) a Yonsei University (YSU) scheme for planetary boundary layer (PBL); and 4) a Rapid Radiative Transfer Model (RRTM) scheme and Dudhia scheme for longwave and shortwave radiation, respectively.

We take initial and boundary conditions from ⅓°, 3-h fields from the NCEP North American Regional Reanalysis [NARR; see Sun and Barros (2012) for discussion of the impacts of forcing datasets on high-resolution tropical cyclone simulations]. The WRF simulation in our study starts at 1800 UTC 26 August 2011, which is 18 h before the first landfall. Our simulation ends at 0600 UTC 29 August 2011, approximately 6 h after the completion of ET.

b. Data

The National Hurricane Center (NHC) "best track" hurricane database (HURDAT) data (6-h interval) from the National Oceanic and Atmospheric Administration (NOAA) Hurricane Research Division (HRD) are used to examine the simulated track of Hurricane Irene. Multiple rainfall datasets are used to develop analyses of rainfall evolution. Stage IV radar rainfall fields are generated from multisensor rainfall analyses by 12 River Forecasting Centers throughout the continental United States (Lin and Mitchell 2005). Stage IV fields are available at hourly time scales with a spatial resolution of approximately 4 km.

Hourly rainfall observations from 77 rain gauges were obtained from the National Centers for Environmental Information [formerly the National Climatic Data Center (NCDC)] and are used to assess WRF-simulated rainfall at individual locations. Rain gauge observations from the Community Collaborative Rain, Hail, and Snow Network (CoCoRaHS; http://www.cocorahs.org/) are also used to examine rainfall distribution, principally in the mountainous northeastern United States. Radar reflectivity fields are obtained from the Newport, North Carolina (KMHX), and Upton, New York (KOKX), Weather Surveillance Radar-1988 Doppler (WSR-88D) radars and used to examine structure of rainbands from Hurricane Irene. We use CG lightning data from the NLDN (see Orville and Huffines 2001; Villarini and Smith 2013)

to examine convective intensity and storm structure of Hurricanes Irene, Hanna, and Sandy.

c. Cyclone phase space analyses of ET

We use the cyclone phase space (CPS) method to study the initiation and completion of extratropical transition (Hart 2003). The CPS method is physically robust and can be implemented using calculations based on geopotential heights at standard pressure levels. It has been used in a wide range of studies to examine the timing of ET (Evans and Hart 2003; Kitabatake 2011; Song et al. 2011; Wang et al. 2012; Griffin and Bosart 2014; Wood and Ritchie 2014). Three time-varying quantities are used in the CPS method. The "asymmetry" parameter B is the 900–600-hPa thickness asymmetry relative to the direction of motion of the storm. Values of thickness asymmetry that are close to 0 indicate a symmetric structure (i.e., a feature associated with TCs), and a large positive value of B indicates extratropical or frontal features. The onset of ET is determined as the time when B first becomes larger than 10 m. The lower thermal wind $-V_T^L$ and upper thermal wind $-V_T^U$ are 900–600- and 600–300-hPa thermal wind values, respectively. Positive values indicate a warm core structure (i.e., associated with TCs), while negative values indicate a cold core structure (i.e., associated with extratropical cyclones). The completion of ET is determined as the first time when $-V_T^L$ is less than zero.

3. Results

a. Hydrometeorological summary of Hurricane Irene

Irene originated as a tropical storm along the western coast of Africa on 15 August 2011 (Avila and Cangialosi 2011). It reached peak intensity as a category 3 hurricane on 24 August in the Bahamas. Irene moved west-northwest as it crossed the Bahamas around 25 August. As Irene approached Florida on 26 August, its evolution was influenced by an approaching trough, and steering to the northeast was initiated.

The track of Hurricane Irene up the East Coast was, in some respects, simple. The storm moved steadily to the northeast, and net storm speed varied relatively slowly during its passage along the East Coast. The WRF simulation generally captures the storm track and speed of Hurricane Irene (Fig. 2). There are small, but significant, differences between the observed and simulated track during the period from 1200 UTC 28 August to 0000 UTC 29 August, which is a period of extreme rainfall and flooding in the Catskill Mountains of New York and in New England. The simulated track deviates slightly eastward from 1200 to 1800 UTC 28 August and

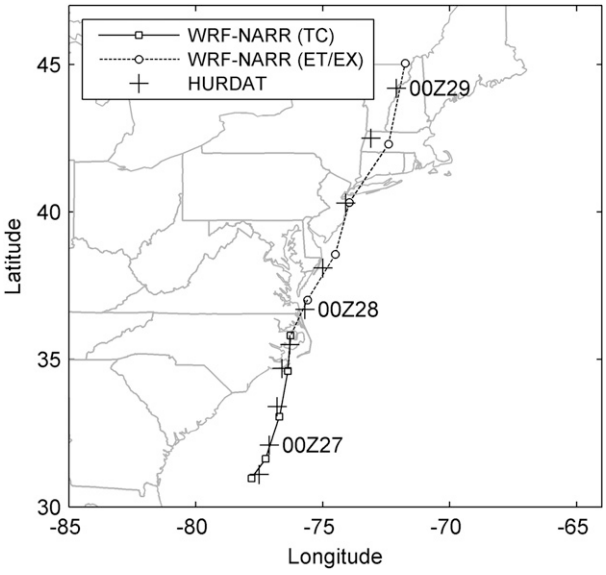

FIG. 2. Tracks of Hurricane Irene from d01 of the WRF–NARR simulation and from HURDAT data. Irene moved from TC stage (solid) to extratropical transition and extratropical cyclone (ET/EX) stage (dashed).

the simulated track moves more rapidly than the observed track from 1800 to 0000 UTC 29 August.

Storm motion was largely controlled by the steering winds associated with the approaching trough. In Fig. 3, we show 1) the observed storm motion (computed as the difference between 6-h locations, centered between the 6-h time periods) and modeled storm motion; 2) steering winds computed as the mean 850–500-hPa wind (speed and direction) averaged over a 500-km radius from the center of circulation of the simulated storm; and 3) wind shear, computed as the difference between the 200- and 850-hPa wind vector, averaged over an annulus extending from 200 to 800 km from the center of the storm. Storm motion is largely oriented along the direction of the steering wind, and the storm speed is generally slightly faster than the speed of the steering wind. An important exception occurred around 1200 UTC 28 August, a period associated with flood-producing rainfall in New Jersey and the state of New York. Storm motion is generally to the left of the shear vector; during the period of rapid increase in wind shear on 28 August, the motion vector is only slightly left of the shear vector.

Irene made initial landfall as a category 1 hurricane around 1200 UTC 27 August near Cape Lookout, North Carolina (Fig. 2). After the initial landfall, Irene continued to move northeastward and made a second landfall as a tropical storm on 28 August at Brigantine, New Jersey (Fig. 2).

CPS analyses of Irene (Figs. 4, 5) exhibit a striking pattern of extratropical transition, which is largely

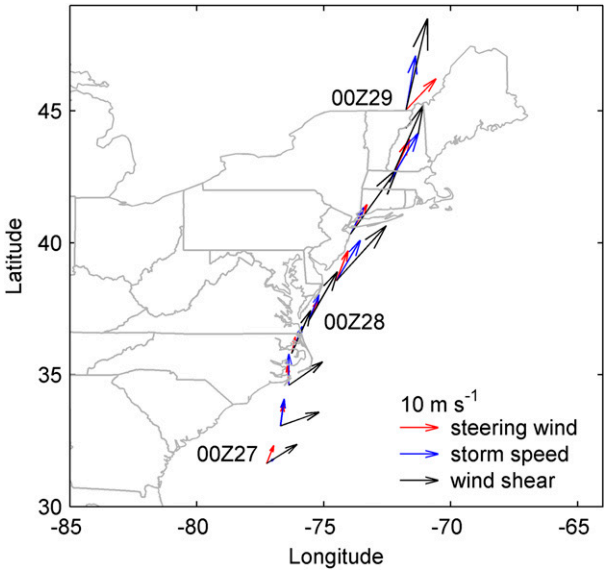

FIG. 3. The 6-hourly steering wind ($m\,s^{-1}$; red), storm speed ($m\,s^{-1}$; blue), and vertical wind shear ($m\,s^{-1}$; black) along the track of Hurricane Irene. The steering wind is defined as the mean 850–500-hPa wind, averaging over a radius of 500 km from the storm center. The wind shear is defined as the mean wind difference between 200 and 850 hPa within an annular area between 200- and 800-km radii from the storm center. The steering wind and shear are based on d01.

matched by Hurricane Hanna in its similar path up the East Coast (Fig. 4; see also additional discussion in section 3e). During the path of Irene up the East Coast, the warm core structure generally intensified until approximately 1400 UTC 27 August. During this period, Irene exhibited symmetric structure, with relatively small variation in the asymmetry parameter. The onset of ET, based on the asymmetry criterion, was at approximately 1700 UTC 27 August. From 1600 UTC 27 August, Irene rapidly transitioned, with a linearly increasing asymmetry and linearly decreasing lower thermal wind. Irene had transitioned from warm core to cold core structure at low levels by 2200 UTC 28 August, completing the process of extratropical transition. The upper-level thermal wind decreased during the period of extratropical transition but remained positive over the entire life cycle (Fig. 5; contrasting with Hurricane Hanna, as discussed in section 3e).

Time evolution of the upper thermal wind generally matched the lower thermal wind (Fig. 5), beginning the decrease with the onset of ET at 1800 UTC 27 August. Lower thermal wind decreased somewhat more rapidly than upper thermal wind during the 12 h after ET was initiated. Lower thermal wind and asymmetry exhibit an increasing slope around 1500 UTC 28 August, during the period of extreme rainfall in New York and New England.

Heavy rainfall from Irene produced extreme flooding along its track over the East Coast and catastrophic flooding in portions of New York and New England. In Fig. 6, we illustrate flood magnitudes through a spatial map of the "flood index," that is, the ratio of the peak discharge to 10-yr flood peak (Smith et al. 2011; Villarini and Smith 2010). The normalized flood peak values from United States Geological Survey (USGS) stream gauging stations are interpolated to a flood peak map (Fig. 6). The map highlights the spatial structure of flooding, with the most severe flooding along the mountains of New York and New England.

The storm total rainfall fields ranging from 0000 UTC 27 August through 0000 UTC 29 August from the WRF

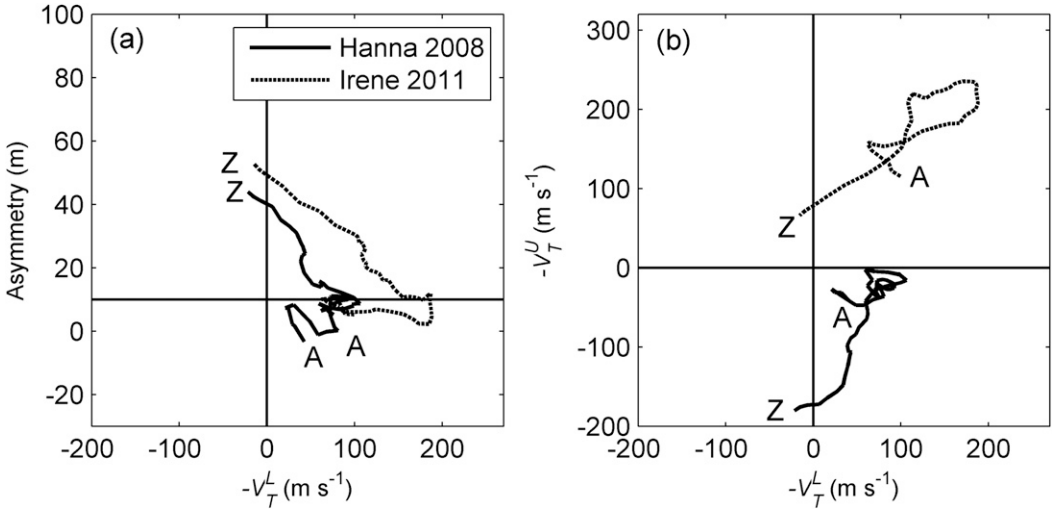

FIG. 4. Cyclone phase space diagrams for Hurricane Hanna (solid) and Irene (dashed) with (a) thickness asymmetry (m) vs $-V_T^L$ and (b) $-V_T^U$ vs $-V_T^L$.

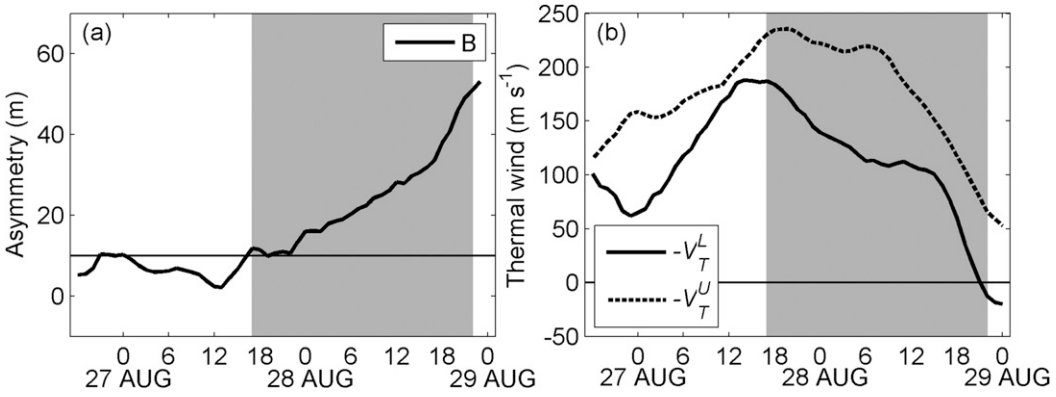

FIG. 5. Time series of (a) thickness asymmetry and (b) $-V_T^L$ and $-V_T^U$ for Hurricane Irene based on CPS method and atmospheric fields from the WRF–NARR run. The gray area indicates the ET period. The two horizontal black lines denote the times when criteria for onset and completion time of ET are satisfied.

simulation and stage IV (Fig. 7) are in good general agreement and also broadly reflect the major features of the flood map (Fig. 6). There are, however, contrasting features between the simulated and observed storm total rainfall fields. The coastal maximum in rainfall at landfall in stage IV is not captured in the simulated rainfall fields. The left-of-track maximum in simulated rainfall, postlandfall (after 1200 UTC 27 August), is less prominently observed in the observed rainfall field, which may be partly attributable to storm center differences around landfall between WRF simulation and best track data. WRF produces a band of rain with a magnitude of approximately 225 mm over the ocean east of North Carolina. This feature is less pronounced in the observed rainfall field for which the coastal maximum is the dominant feature of the spatial distribution of rainfall. Observed rainfall in the mid-Atlantic region generally has a rainfall maximum along the track, while the simulated rainfall fields have a slight left-of-track distribution of maximum rainfall.

Simulated rainfall fields from WRF also capture the broad features of the temporal evolution of rainfall fields. In Fig. 8a, we show a scatterplot of hourly gauge rainfall with WRF rainfall (for the grid containing the rain gauge). To reduce spatial sampling errors, hourly gauge rainfall is matched with average hourly rainfall from the WRF grid containing the target grid as well as the nearest eight grids. Hourly rainfall totals from the WRF simulation match well with hourly gauge rainfall, with a correlation coefficient of 0.62 and root-mean-square error (RMSE) of 4.39 mm h^{-1}. In Fig. 8b, we show time series of mean rainfall from all rain gauges and mean stage IV and WRF rainfall at rain gauge locations. These results suggest that the WRF simulation captures the main features of rainfall distribution in space and time.

The WRF simulation captures the time evolution of mean rainfall and rain area (Fig. 9), following the track of the storm. In Fig. 9, we show time series of mean rainfall for the inner core region (<100 km; Fig. 9a) and for the outer core region (100–300 km; Fig. 9b). We also present time series of the fractional area (within 300-km radius) with rainfall rate exceeding 1 mm h^{-1} (Fig. 9c) and 5 mm h^{-1} (Fig. 9d). There is particularly good agreement between model and observations for mean rainfall within 100 km of the storm. There is a pronounced peak in mean rainfall within 100 km around 1600 UTC 27 August in both observed and simulated rain fields. Overestimation of rainfall in model simulations is principally for the outer band region (Fig. 9b), and the observed and model mean rainfall time series for the outer band region remain relatively constant over the storm life cycle. Rain area for both 1 and 5 mm h^{-1} thresholds increases steadily over much of the storm life cycle. There

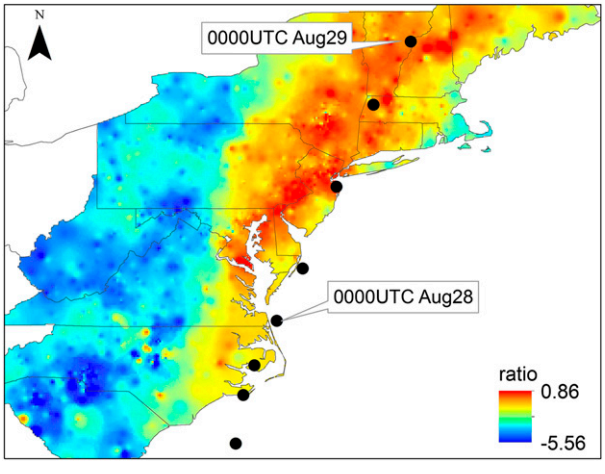

FIG. 6. Flood index, that is, the ratio of peak discharge to 10-yr peak discharge for Hurricane Irene. Analyses are based on flood peak observations from 1831 USGS stream gauging stations.

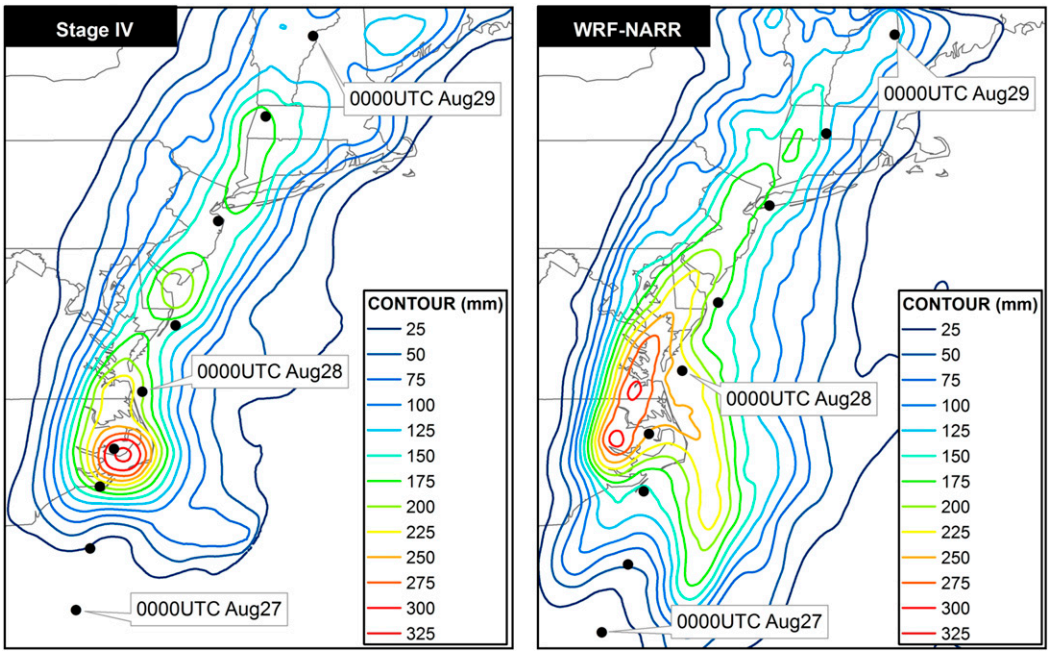

FIG. 7. Storm total rainfall (mm) for Hurricane Irene from (left) stage IV radar rainfall fields and (right) WRF–NARR simulation. The time period is from 0000 UTC 27 Aug to 0000 UTC 29 Aug. Locations of the center of circulation of the storm are indicated by black dots from WRF–NARR (3 hourly; left) and best track data (6 hourly; right).

is a systematic overestimation of rainfall area for the 1 mm h^{-1} threshold and a decreasing overestimation with time for the 5 mm h^{-1} threshold.

b. *Evolution of the spatial and temporal rainfall distribution*

The temporal evolution of the spatial distribution of rainfall from Hurricane Irene is examined following procedures introduced in Villarini et al. (2011). The rainfall distribution is examined through the azimuthally averaged rainfall as a function of distance from the storm center (Fig. 10). Following the track of Irene, the rainfall domain is divided into four quadrants with respect to the storm motion: left front, right front, left back, and right back. For each hour, we characterize the radial rainfall distribution over each quadrant instead of

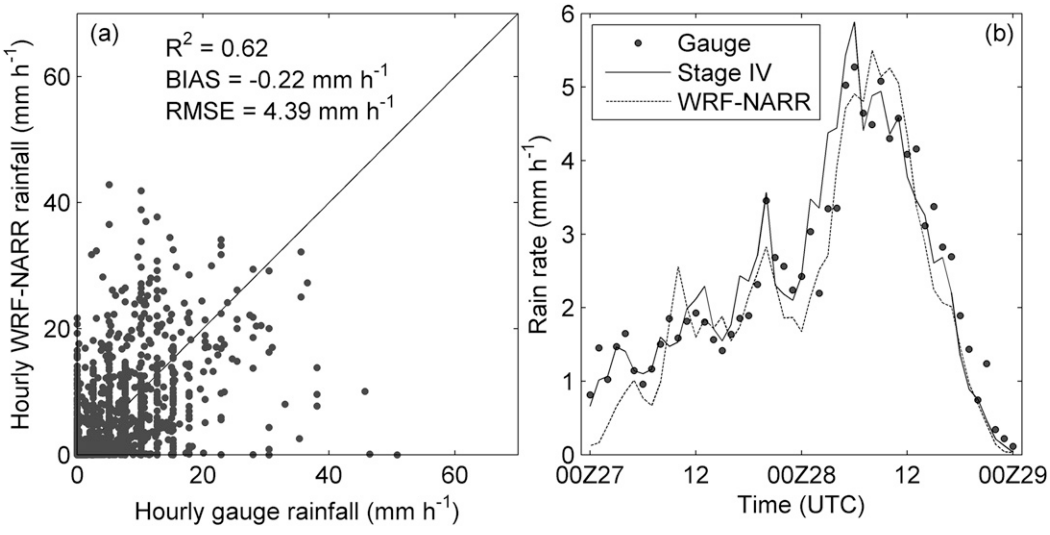

FIG. 8. (a) Scatterplot of hourly rainfall of Hurricane Irene from rain gauges and from the WRF–NARR simulation, using the grid containing rain gauge and (b) time series of mean rainfall from all gauges, stage IV, and WRF–NARR at all corresponding gauges.

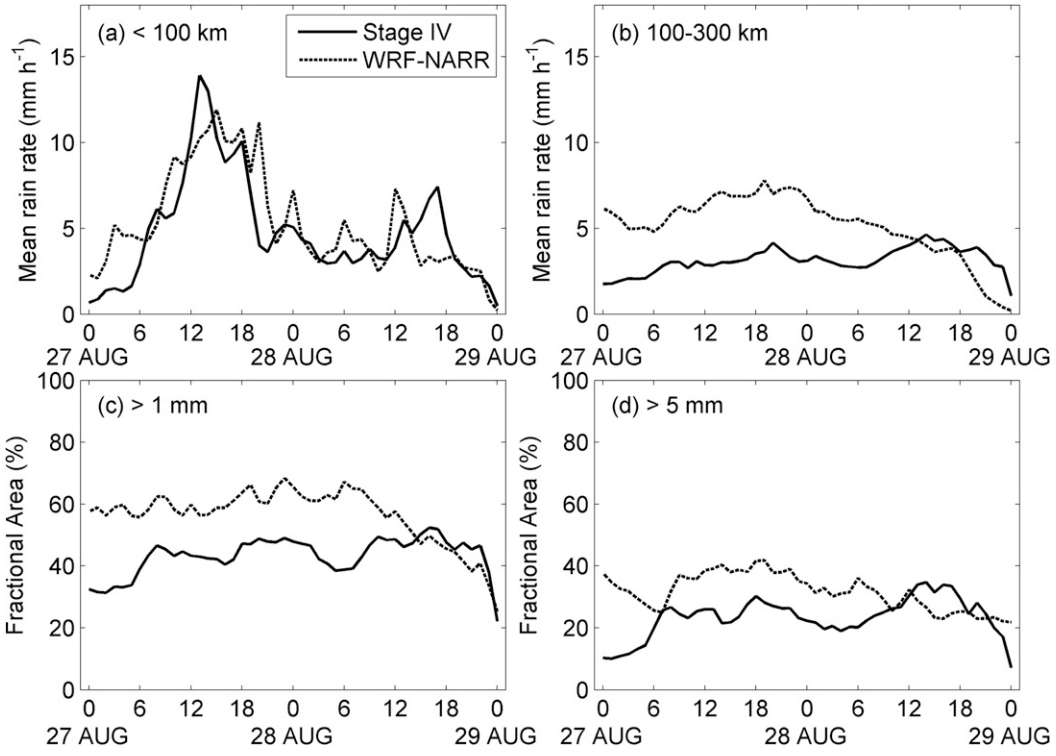

FIG. 9. Time series of mean rainfall of Hurricane Irene for radii of (a) 100 km and (b) 100–300 km from the storm center and fraction area with rainfall exceeding (c) 1 mm and (d) 5 mm within a radius of 300 km from the storm center.

averaging over a 360° azimuth. This quadrant analysis provides a useful tool to analyze the spatial and temporal variability of rainfall structure.

Rainfall from Irene was generally concentrated in the left-front quadrant in both observed and simulated rainfall fields, except that the WRF simulation produces large rainfall magnitudes in the right-front quadrant around the first landfall. From 0000 UTC 27 August to the first landfall, rainbands in the left-front quadrant from both stage IV and WRF move toward the storm center, although the observed fields exhibit rainbands closer to the storm center and with higher rain rates than the simulated fields.

Around the first landfall, both observed and simulated rainfall fields exhibit rainfall increases in the left-front quadrant but show contrasting rainfall structure. The rainfall increase in stage IV is mainly within a radius of about 180 km from the circulation center. The peak rainfall is located within 60 km from the storm center with rain rates around 60 mm h^{-1}. The dominant rainbands simulated by WRF are more than 60 km from the storm center and have lower peak rain rates than stage IV. Compared to rainfall in the left-front quadrant, stage IV exhibits similar rainfall increase in the right-front quadrant but with lower rain rates and smaller coverage. In the right-front quadrant, the WRF simulation shows heavy rainfall over the ocean. This rainband is not a prominent feature of the observed rainfall fields.

From the first landfall to the second landfall, observed rainfall fields from stage IV exhibit rainbands that are moving away from the storm center in the left-front quadrant. Simulated rainfall fields from WRF show a similar pattern, but with much larger rain rates. After the second landfall, stage IV shows rainfall increases in the left-front quadrant with peak rain rates around 18 mm h^{-1} within a distance of 140 km from the center. The rainfall increase may be related to topographic effects because it corresponds to the time when the center of Irene reaches the central Appalachians. The topographic impact on rainfall will be further discussed in section 3d. A similar rainfall pattern is also found in the WRF simulation.

Another common feature of the two rainfall fields is that very little rainfall is produced in the right-front quadrant from around 1800 UTC 27 August to the second landfall time. Physical processes linked to ET play a role in this feature of rainfall distribution, as discussed in the next section. In summary, the WRF simulation captures the concentration of Irene rainfall in the left-front quadrant but is generally ''wetter'' than observed rainfall fields from stage IV.

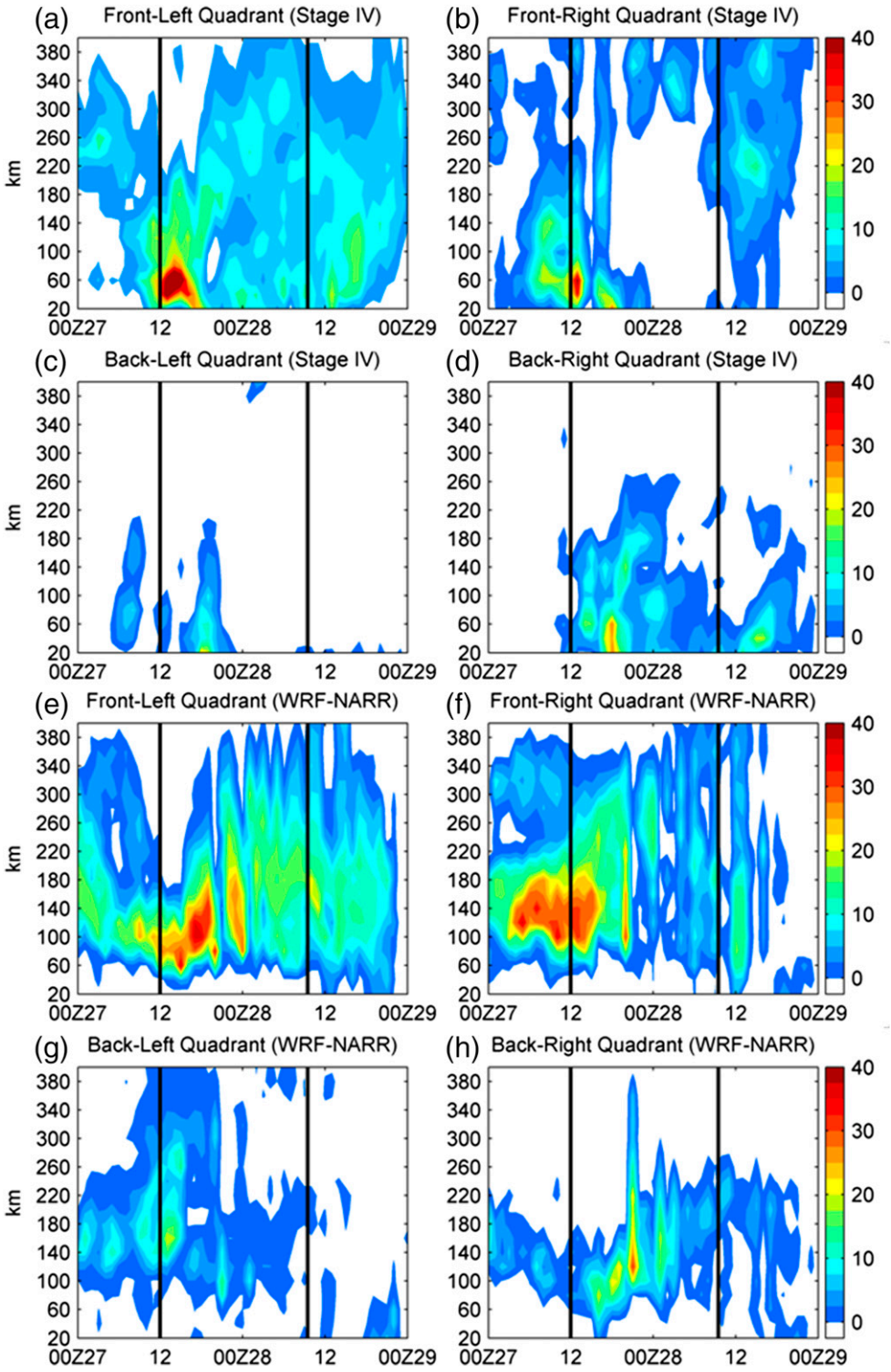

FIG. 10. Rainfall distribution as a function of distance from the storm center of Hurricane Irene and time, based on (a)–(d) stage IV radar rainfall fields and (e)–(h) WRF–NARR simulation. The four quadrants are defined with respect to the direction of propagation of Irene. The black lines indicate the time of landfall, that is, 1200 UTC 27 Aug and 0935 UTC 28 Aug, respectively.

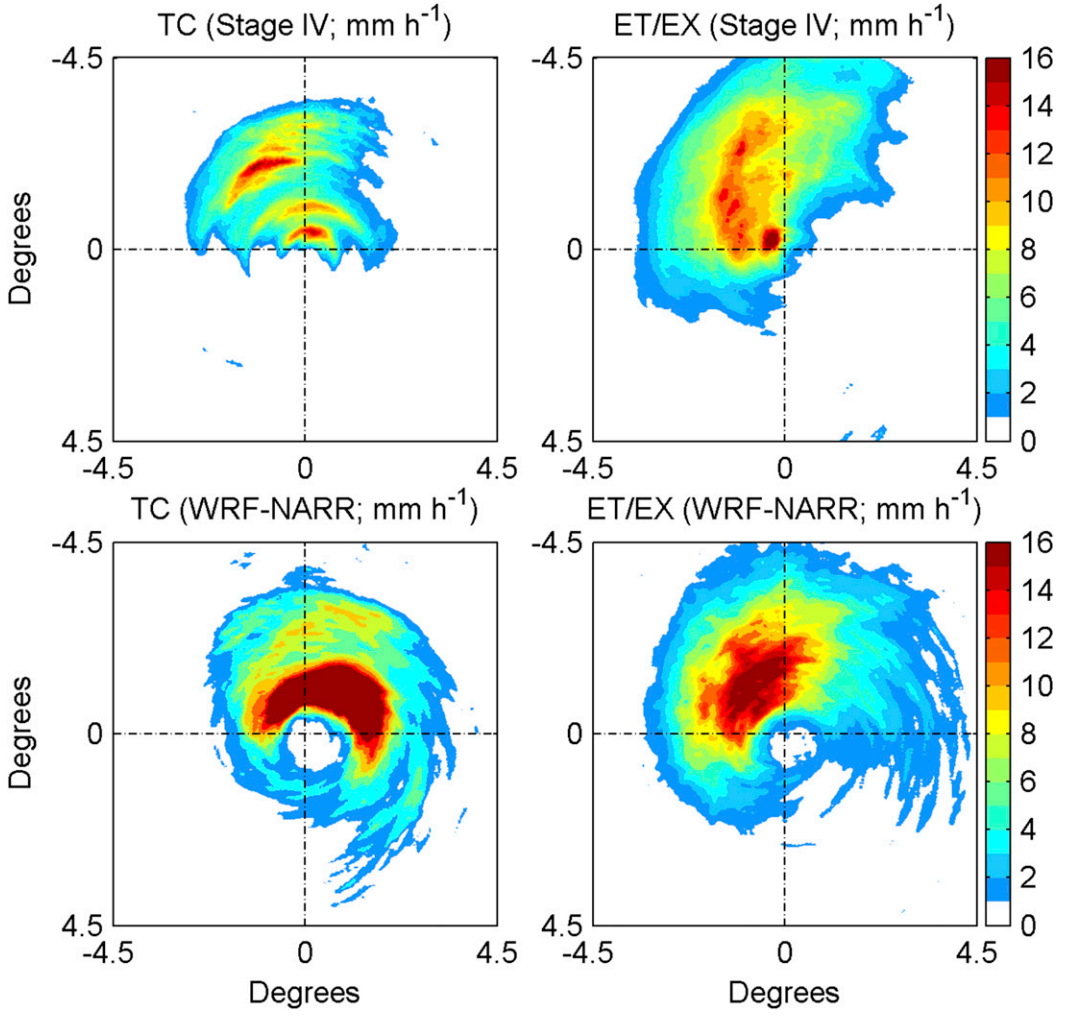

FIG. 11. The rainfall composite of (top) stage IV and (bottom) WRF–NARR rainfall during TC and ET/EX stages for Hurricane Irene, respectively.

c. *Rainfall evolution and ET*

To explore the impact of ET on the evolving rainfall structure of Irene, we divided the storm into two periods: before and during ET. For each period, the hourly rainfall pattern is rotated around the storm center so that its direction of motion corresponds with the north axis. The hourly rainfall distribution is then averaged relative to the storm center. The contrast of the two storm-motion-relative rainfall composites highlights the impact of ET on rainfall organization (Fig. 11).

Before ET, stage IV rainfall shows three distinct spiral rainbands around the storm center. These bands are located in the front quadrants of Irene and stretch from the east to the west. During ET, stage IV rainfall is mainly concentrated in the left-front quadrant and more evenly distributed instead of forming spiral rainbands in the pre-ET period. Compared to observed rainfall fields, simulated rainfall shifts from right-of-track to left-of-track distribution as Irene moves from pre-ET to the ET period.

Before ET, WRF shows a large rainband with a rain-rate magnitude larger than 20 mm h^{-1} in the right-front quadrant, which is dominated by rainfall produced over the ocean. Observed rainfall fields do not reflect this aspect of heavy rainfall, as discussed in the previous section. During ET, WRF captures the left-front quadrant distribution of rainfall but is wetter than observed rainfall.

As reflectivity is extensively used in TC rainfall studies involving observations and simulations (e.g., Didlake and Houze 2009; Akter and Tsuboki 2012; Bao et al. 2015; Moon and Nolan 2015), we focus on instantaneous reflectivity fields at 1200 UTC 27 August (Figs. 12a,b) and at 0900 UTC 28 August (Figs. 12c,d) to provide a detailed depiction of the storm structure. Observed

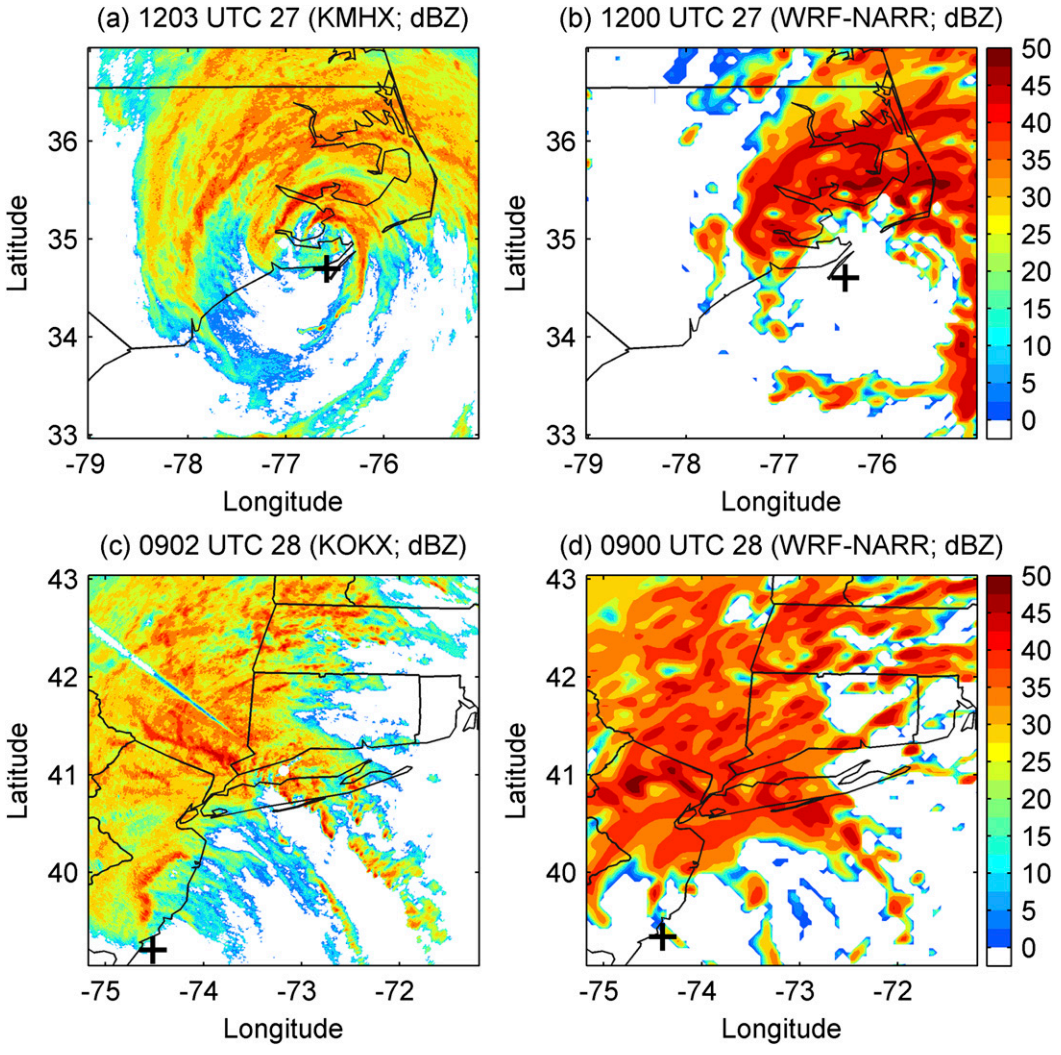

FIG. 12. Radar reflectivity (dBZ) fields of Hurricane Irene at 1-km height at (a) 1203 UTC 27 Aug (KMHX) and (c) 0902 UTC 28 Aug (KOKX). Simulated 850-hPa reflectivity fields from WRF–NARR at (b) 1200 UTC 27Aug and (d) 0900 UTC 28 Aug are also indicated. The plus sign shows the location of the storm center.

reflectivity fields are from KMHX for 1200 UTC 27 August and from KOKX for 0900 UTC 28 August. The 850-hPa reflectivity fields from the WRF simulation are shown for comparison. At the time of the first landfall (Fig. 12a), rainfall is organized into a sequence of rainbands extending from the eyewall to a radius of slightly more than 100 km from the storm center. The rainbands are almost exclusively restricted to the forward sector of the storm. The innermost rainband is the exception, with rainfall wrapping from the back right sector of the storm counterclockwise to the front sector. The concentration of rainfall shifts progressively to the front left sector for the rainbands at farther distance from the center of circulation.

Like the observed reflectivity field, the WRF reflectivity field at 1200 UTC 27 August (Fig. 12b) has a distribution of rainfall concentrated in the forward sector of the storm and an inner rainband that wraps around the center of circulation of the storm from the right-back sector to the forward sector of the storm. The simulated reflectivity field does not reflect the details of rainband structure in the observed reflectivity field and the magnitudes of reflectivity are greater than the observed values.

The reflectivity structure at the time of the second landfall (0900 UTC 28 August; Fig. 12c) is strikingly different from the structure 21 h earlier at the first landfall. Rainfall is concentrated in bands that extend from southeast to northwest at distances more than 100 km from the center of circulation. The observed and simulated rainfall accumulations for this period are concentrated in the forward sector of the storm

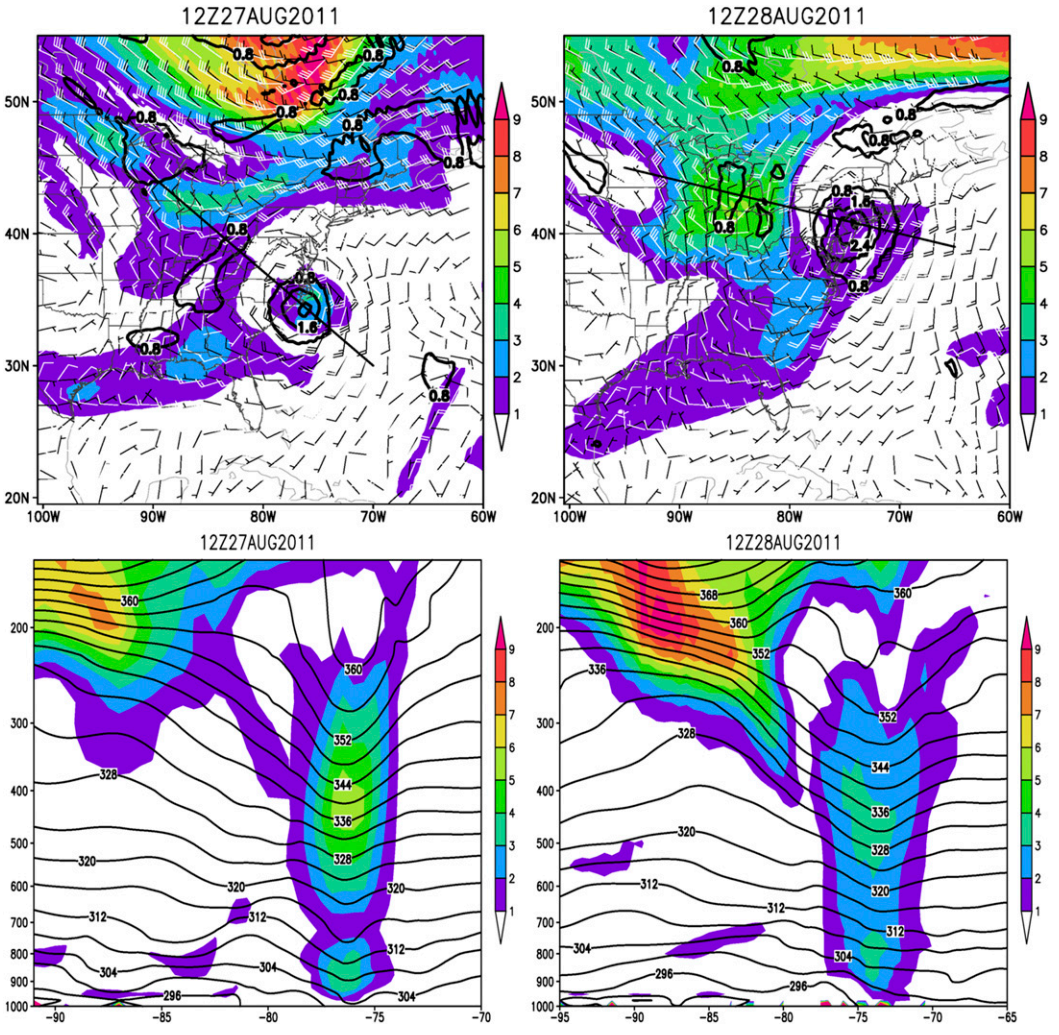

FIG. 13. (top) The 300–200-hPa PV (PVU; 1 PVU = 10^{-6} K kg^{-1} m^2 s^{-1}; shaded) and wind (m s^{-1}; white barbs) with the 850–700-hPa PV (PVU; black solid contours) and wind (m s^{-1}; black barbs) overlaid. (bottom) Cross sections [locations denoted by thick black lines in (top)] of PV (PVU; shaded) and potential temperature (K; black contours). This analysis of Hurricane Irene is based on NARR data.

(figure not shown). The structure of simulated rainbands, however, does not match those of the observed rainbands (Figs. 12c,d).

To understand the fundamental change of rainfall structure before and during ET, the synoptic-scale environment of Irene is examined from the PV perspective. As shown in Fig. 13, at 1200 UTC 27 August, an upper-level trough was located to the northwest of Irene with strong southwesterly/westerly jets. Although baroclinicity indicated by the horizontal potential temperature gradient in the cross section was clearly seen between the trough and Irene, Irene remained as a separate tropical cyclone with a near-zero thickness asymmetry and positive thermal wind as shown in the CPS analyses (Fig. 5). After 24 h, Irene was closer to the trough as it moved northward. The enhanced downstream ridge shifted the orientation of the trough from neutral to negative (from northwest to southeast) and displaced Irene into an upper-level jet stream region. As seen in the cross-sectional map, the location of the trough was around 200 hPa at 1200 UTC 27 August and moved down to 300 hPa after 24 h, showing the strengthening of potential temperature gradient and thus baroclinicity, which was consistent with the trend of increased asymmetry thickness and decreased thermal wind in the during-ET period (Fig. 5).

The increasing vertical wind shear, beginning around 1800 UTC 27 August (Fig. 14), also affects rainfall distribution during the ET period. Magnitude of wind shear increased from approximately 12 m s^{-1} at 1800 UTC 27 August to more than 20 m s^{-1} by 1200 UTC 28 August. There may be low-level inward flow and upper-level

outward flow associated with wind shear in the downshear side. It causes negative (positive) vorticity advection in the lower (upper) atmosphere, which produces low-level convergence and upper-level divergence through the vorticity conservation constraint and promotes a secondary circulation in the downshear side (Gao et al. 2009; Xie and Zhang 2012). The wind shear time series of Irene is shown in Fig. 14. The wind shear showed an increasing trend over time and the increase accelerated after 1200 UTC 28 August, which may be due to the strong upper-level jet from the trough. The wind shear was directed to the north-northeast of Irene, providing another important element of rainfall concentration in the left-front quadrant of Irene during the ET period.

d. Orographic rainfall

The WRF simulation produced rainfall amounts exceeding 150 mm in New York and New England (Fig. 7). Orographic precipitation enhancement in the Appalachians is examined through the comparison of two WRF simulations: the control run with original terrain and the nonterrain run with flat terrain. The daily rainfall distribution from CoCoRaHS rain gauges from ~1100 UTC 28 August to ~1100 UTC 29 August are used to assess the simulations of rainfall from the control run and nonterrain run. Although the time period for control and nonterrain runs ends at 0000 UTC 29 August, the rainfall accumulations in the study region are quite small after the time because the storm moves out of New England.

The daily rainfall difference between observations from CoCoRaHS and the nonterrain run (Fig. 15) shows that rainfall underestimates can be as large as 80 mm in Vermont and New York, highlighting the orographic effect in rainfall production. The rainfall overestimation extending from Connecticut to Massachusetts may result from the time lag of the track. The storm center in the nonterrain run moves more slowly than the control run and thus allows more time for the nonterrain run to produce rainfall in southern New England. The track location differences from the two simulations are relatively small (figure not shown), but contribute to rainfall differences between the two simulations. The steering wind in the nonterrain run is steadily lower than the control run (figure not shown), suggesting that the large-scale environmental wind could be important in impacting the storm speed of Irene. The nonterrain run underestimates rainfall in New York, with especially large underestimates in the Catskill Mountains, which experienced extreme flooding.

The strong rainfall across Vermont produced flash flooding that caused extended damage to bridges, roads,

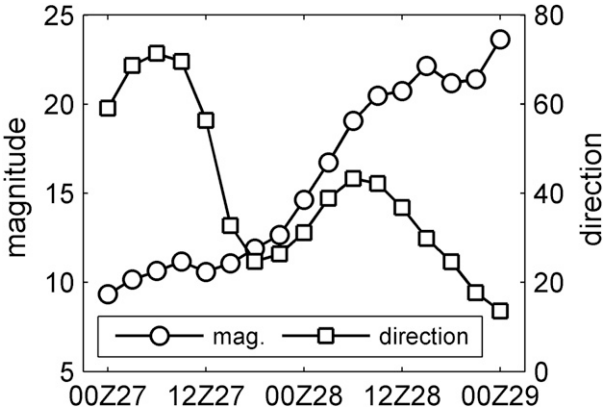

FIG. 14. Time series of vertical wind shear with magnitude ($m\,s^{-1}$) and direction (°) for Hurricane Irene. The direction is the anticlockwise angle from the north. The shear is the same as that in Fig. 3.

and homes (Avila and Cangialosi 2011). We explore orographic rainfall mechanisms in this region by assuming that forced uplifting is a key mechanism of orographic rainfall as Irene passed across the mountain ridge (Fig. 16a) in Vermont. We use a simple one-dimensional (1D) model (Smith 1979) to understand the first-order rainfall magnitude from the interaction between the mountain ridge and Irene. In a saturated adiabatic environment, the condensation rate is approximated by the decreasing rate of saturated water vapor density:

$$\frac{\partial \rho_{vs}}{\partial t} = -w\frac{\partial \rho_{vs}}{\partial z}, \tag{1}$$

where ρ_{vs} is the saturated water vapor density, t is the time, z is the height, and w is the vertical wind speed. Assuming that the formed raindrops from condensed droplets immediately fall down to ground without horizontal drifts, the rain rate is approximated as the vertical integral of the decreasing rate of saturated vapor density:

$$R = \int_0^H -w\frac{\partial \rho_{vs}}{\partial z}dz, \tag{2}$$

where H is the top integral height. In the case of upslope lifting, the vertical motion is only forced by topography. In a flow "climbing" the windward slope of a mountain, vertical speed is approximated as

$$w = u \times \mathrm{slp}, \tag{3}$$

where u is the horizontal wind and slp is the slope. As Irene moved north toward Vermont, the front sector began to interact with the mountain ridge specified in Fig. 16a. To be consistent with the assumption of

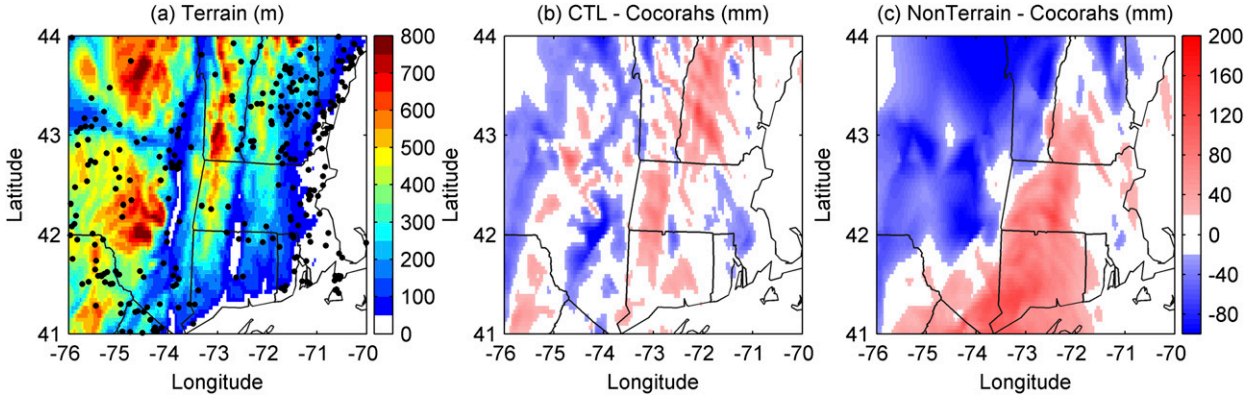

FIG. 15. (a) The terrain height (m; shaded) and CoCoRaHS rain gauges (black dots). Daily rainfall difference (mm) between (b) control run (CTL) and (c) nonterrain run CoCoRaHS rain gauges for Hurricane Irene. The rain period for CoCoRaHS rain gauge observations is from 1100 UTC 28 Aug to 1100 UTC 29 Aug. The rain period for both CTL and nonterrain run is from 1100 UTC 28 Aug to 0000 UTC 29 Aug.

saturated air, the top integral height is confined to 400 hPa in which the relative humidity is generally larger than 80%. All variables are horizontally averaged in the specified region to compute the average rainfall.

The rain rate from the 1D model is comparable to WRF–NARR simulation, showing that the upslope lifting could be a key mechanism in rainfall production (Fig. 16b). Increasing underestimation of rainfall in the 1D model is found over time, which may be due to increasing rainfall production from extratropical transition as Irene moved closer to the trough in the northwest. Examination of Froude number (Fr = U/NH, where U is the wind speed, N is the Brunt–Väisälä frequency, and H is the mountain height) in this region can further support precipitation enhancement through orographic lifting on the windward side (Yu and Cheng 2013). Here U and N are the average 900–850-hPa zonal wind and Brunt–Väisälä frequency in the specified region, respectively. The average mountain ridge height is approximately 800 m, which is used to represent H. As shown in Fig. 16c, the low-level Froude number is larger than the critical value of unity, so supercritical flow from Irene can climb over the mountain, which further highlights the impact of the upslope lifting mechanism on orographic rainfall.

e. Comparison to Hurricanes Hanna and Sandy

In this section, we compare rainfall distribution from Hurricane Irene to Hurricane Hanna, which had a similar track to Irene along the East Coast (Fig. 17), and Hurricane Sandy, which had a track normal to the coast [Fig. 17; see Lin et al. (2010) for related analyses of Hurricane Isabel]. We carried out WRF simulations for Hurricanes Hanna and Sandy using similar model configuration to the Irene simulations.

Despite the similarities in their tracks, there are pronounced contrasts in the rainfall distribution between Hurricanes Irene (Fig. 7) and Hanna (Fig. 17). Most

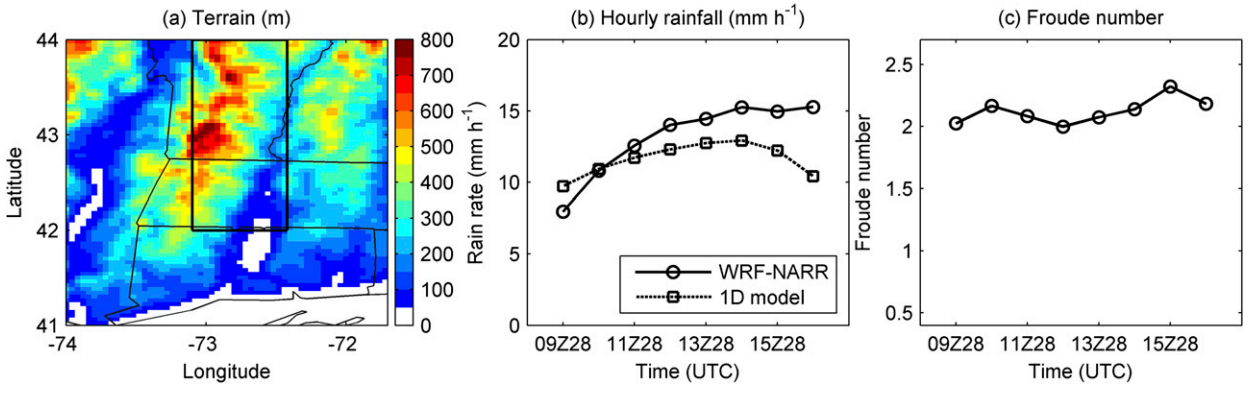

FIG. 16. (a) The terrain height (m; shaded), (b) the hourly rainfall series (mm h^{-1}) of the WRF–NARR run and the 1D model, and (c) the 900–850-hPa Froude number. The WRF–NARR hourly rainfall is averaged from the region indicated by the rectangle box in (a). The 1D model rainfall and Froude number are computed from the same area.

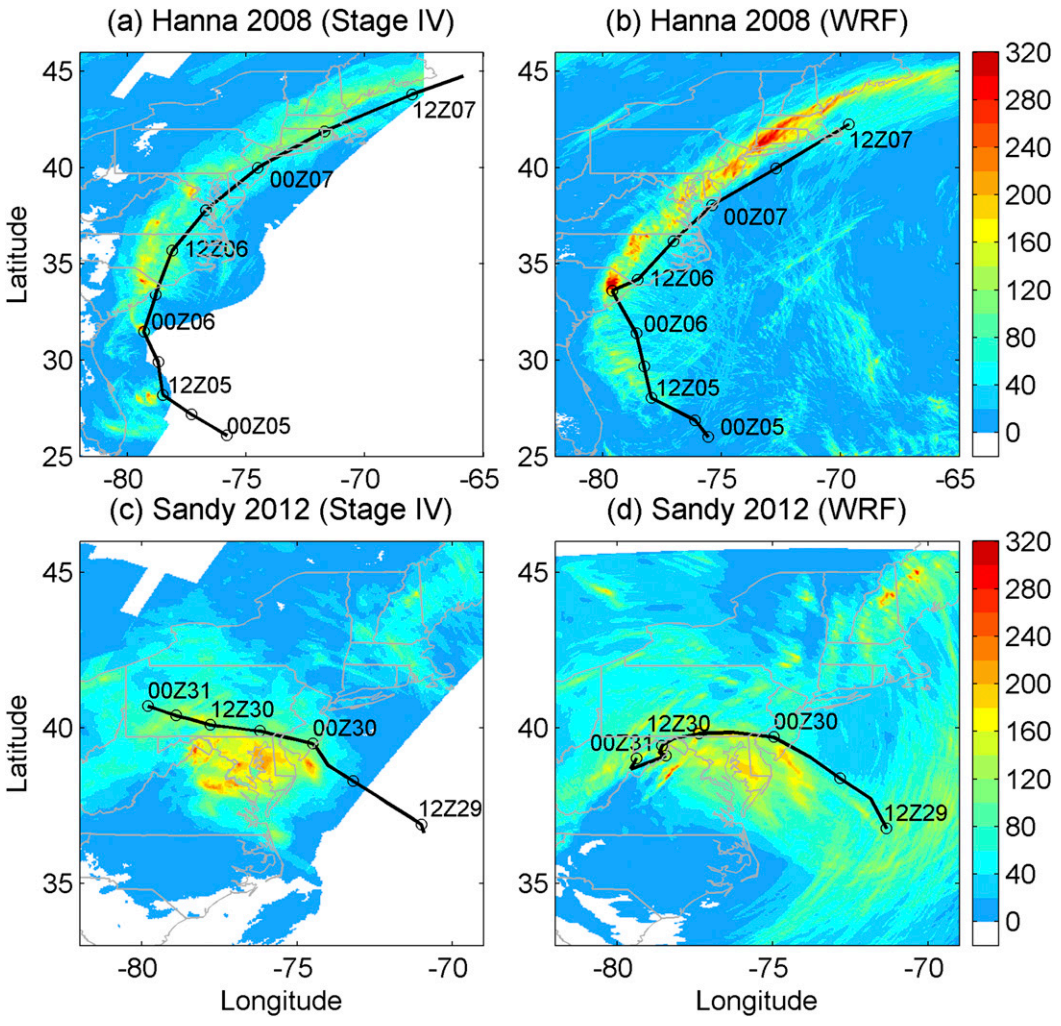

FIG. 17. Storm total rainfall (mm; shaded) for Hurricanes (a),(b) Hanna and (c),(d) Sandy from stage IV radar rainfall fields and WRF simulations. Locations of the storm center of the storms are indicated using (left) best track data (6 hourly) and (right) WRF simulations (6 hourly).

notably, heavy rainfall from Hanna was organized into ''small'' regions of intense convective rainfall. Flash flooding in the Washington, D.C., area was associated with one of the local maxima in rainfall. Like Irene, rainfall from Hanna generally exhibited a left-of-track organization (Figs. 18, 19), but rainfall from Hanna, in both observed and simulated fields, was generally distributed closer to the center of circulation of the storm than in the case of Irene. The left-of-track distribution of rainfall for Hanna is structurally similar before and during ET (Fig. 19), both in observed and simulated rainfall fields. The magnitudes of rainfall are greater during the ET and extratropical periods.

Cyclone phase space analyses of extratropical transition for Hurricane Hanna are similar to those for Irene, with increasing low-level, warm core structure preceding the period of extratropical transition, followed by a near-linear decrease of the low-level thermal wind and increase in asymmetry (Fig. 4). The striking contrast between Irene and Hanna, however, is in the upper-level thermal wind, with Hanna showing cold core structure throughout its path up the East Coast (Fig. 4). The difference of vertical temperature profile between the two hurricanes suggests that Hanna may have higher convective instability in the inner core than Irene, which is further explored using convective available potential energy (CAPE). Hanna shows CAPE larger than 2000 J kg^{-1} in the inner region while the high CAPE area of Irene is concentrated on the right sector (figure not shown).

The difference of the spatial distribution of CAPE in the two hurricanes is consistent with the striking contrast between Hanna and Irene in convective intensity of rainfall, as represented by CG lightning strikes (Fig. 20). Hanna was a prolific lightning producer in the inner

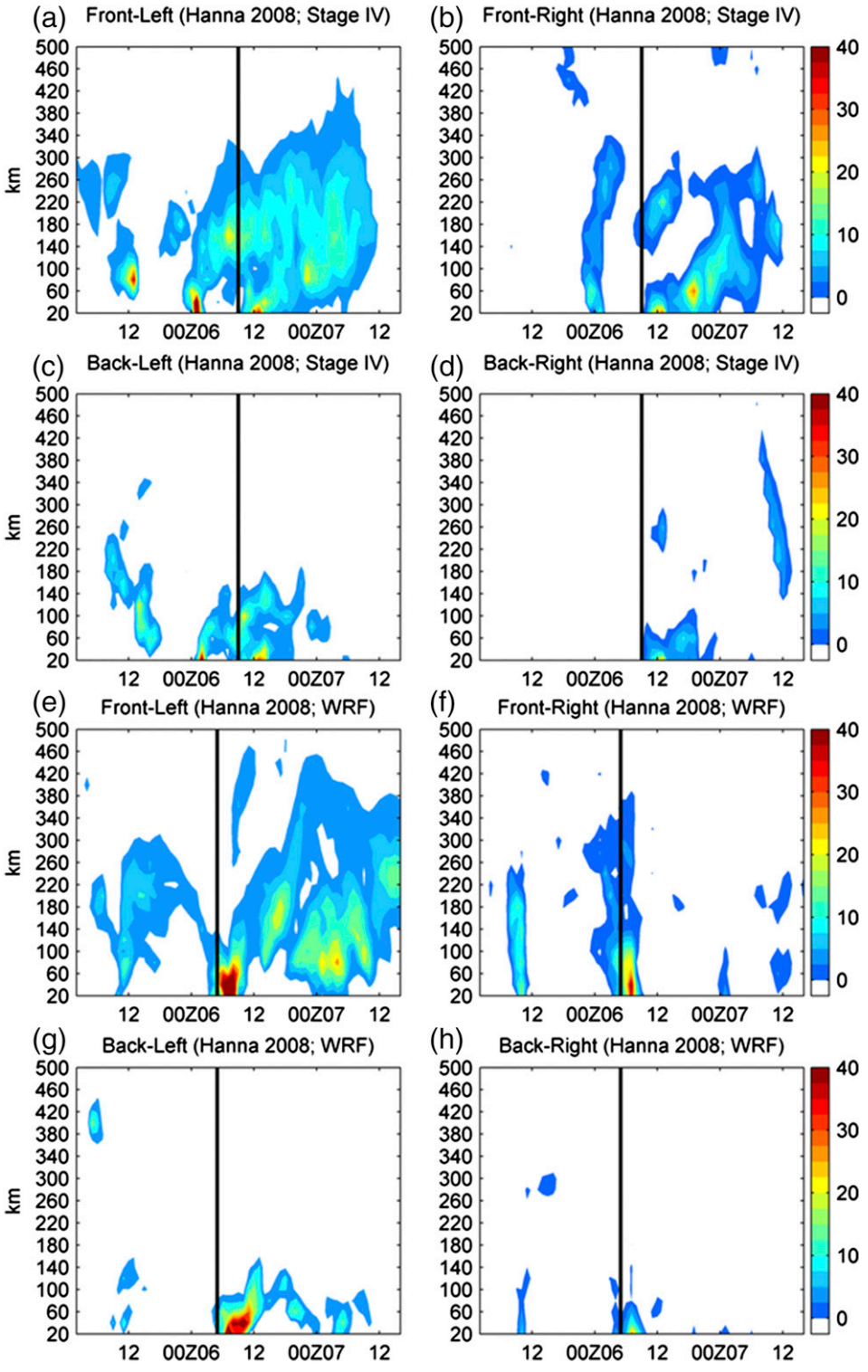

FIG. 18. As in Fig. 10, but for Hurricane Hanna. The black lines indicate the time of landfall, that is, 0900 UTC 6 Sep for best track and 0500 UTC 6 Sep for WRF run.

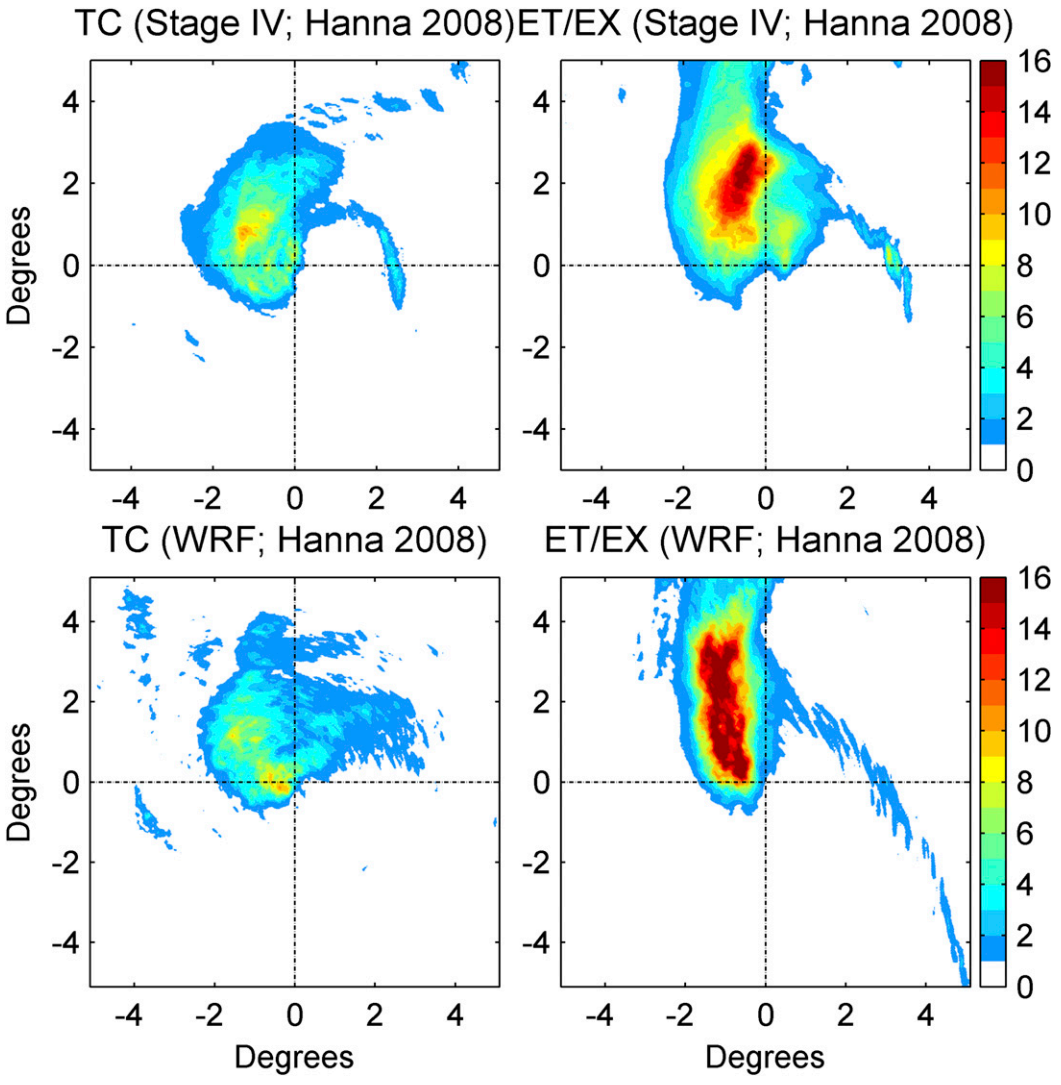

FIG. 19. The rainfall composite of (top) stage IV and (bottom) WRF simulation for Hurricane Hanna rainfall during TC and ET/EX stages, respectively.

region of the storm before landfall. The local maximum in rainfall that occurred shortly after landfall just south of the North Carolina–South Carolina border (Fig. 20) was associated with large lightning flash density in the inner region of the storm, left of the track. The local maximum in rainfall is even more pronounced in the WRF simulation than in the observed rainfall field. Clusters of CG lighting occurred along the track of Hanna along its path up the East Coast. Elevated CG lightning flash densities in New Jersey were associated with convectively intense rainbands that produced locally heavy rainfall rates. The temporal pattern of rainfall rate at any location, like the spatial pattern of rainfall, was highly variable.

Lightning production for Hurricane Irene was concentrated in outer rainbands over ocean in the right-front quadrant of the storm on 27 August (Fig. 20). Unlike Hanna, there was virtually no lightning in the inner region of the storm. Lightning was also principally located in the downshear right quadrant (Figs. 3, 20) on 27 August (see Corbosiero and Molinari 2002, 2003), although lightning extended from the right-back to left-front quadrants, relative to the shear vector. As the storm passed through New Jersey and into New England on 28 August, rainbands produced lighting along the Catskills and in New England. Rainfall responsible for record flooding in the Catskills and New England, however, was associated with weak convection and stratiform precipitation amplified by orographic precipitation mechanisms.

Hurricane Sandy is best known for storm surge flooding along the East Coast, but it also produced

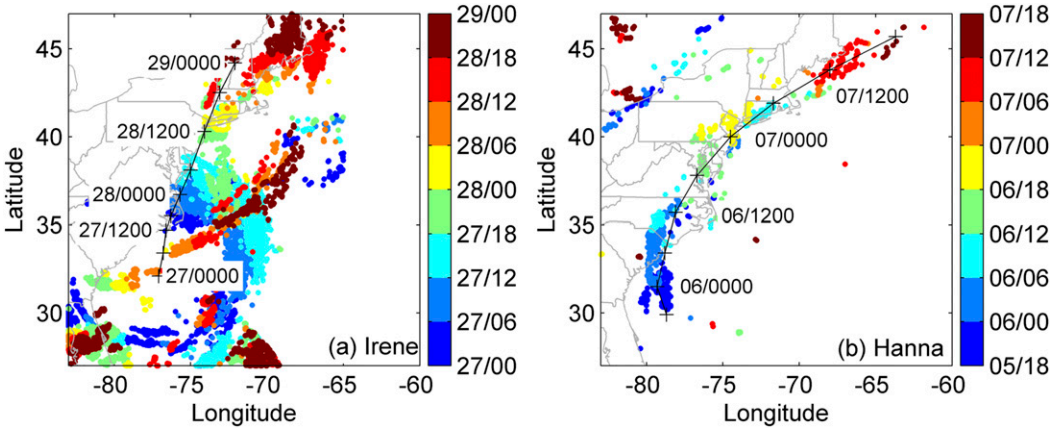

FIG. 20. Locations of lightning from (a) Irene and (b) Hanna, respectively. The color indicates time.

heavy rainfall (Fig. 17) and moderate flooding in the mid-Atlantic region. Like Hurricane Isabel in 2003 (Lin et al. 2010), the track of Sandy was normal to the coast line and the storm moved west through the mid-Atlantic region. Sandy transitioned rapidly from a warm core, symmetric storm to a storm with pronounced asymmetry (figure not shown). During this period, the warm core structure of the storm increased somewhat. Subsequently, Sandy transitioned rapidly to a cold core structure, but during this phase the asymmetry decreased steadily. Sandy retained upper-level warm core structure throughout its life cycle (figure not shown).

Rainfall from Sandy was concentrated left of track (Figs. 17, 21) and in the front quadrant (Figs. 21, 22) of the storm. Rainfall accumulations ranged from 100 to 250 mm over an east-to-west-oriented domain from Delaware through Maryland, northern Virginia, and West Virginia. The Potomac River at Point of Rocks (drainage area of 25 000 km^2) experienced an annual flood peak from Sandy; the 3000 $m^3 s^{-1}$ peak discharge has a return interval of approximately 2 years. Simulated rainfall (Fig. 17) matches the west-of-track orientation of the observed rainfall field and the range of storm total rainfall magnitudes is comparable to the observed storm total field. The simulated rainfall field shows a pronounced maximum in rainfall along the Blue Ridge Mountains, which is not reflected in the observed rainfall field. Observed rainfall has maximum accumulations in the central Appalachian Mountain region, but there is not a pronounced concentration of rainfall on the eastern ridge of the region, as appears in the WRF simulation.

Storm tracks that move from east to west along the East Coast, like Hurricane Sandy (and Isabel; see Lin et al. 2010), will typically have space–time rainfall distributions that move "up" the east-draining rivers of the region (notably, the James, Potomac, and Susquehanna Rivers). Storms like Irene and Hanna that move predominantly from south to north along the East Coast will cross the major Atlantic drainages. These are two extremes in a spectrum of storm tracks. Tropical cyclone structure and motion are important determinants of scale-dependent flood response for the eastern United States [see Sturdevant-Rees et al. (2001) for analyses of the interplay between storm structure, drainage network structure, and flood response for Hurricane Fran in 1996].

4. Summary and conclusions

We examine the temporal and spatial distribution of rainfall from landfalling tropical cyclones through analyses of high-resolution simulations and observed rainfall fields for Hurricane Irene (2011). We compare the space–time evolution of rainfall for Hurricane Irene with a tropical cyclone, Hurricane Hanna (2008), which exhibited a similar track up the U.S. East Coast and with Hurricane Sandy (2012), which also produced heavy rainfall and inland flooding in the eastern United States, but exhibited a very different track. Principle conclusions are summarized as follows.

1) Hurricane Irene produced extreme rainfall and flooding along the U.S. East Coast, with the most extreme flooding extending from New Jersey through the Catskill Mountains of New York and into New England. High-resolution simulations with WRF capture important features of the rainfall distribution, based on intercomparisons with stage IV radar rainfall fields and hourly rain gauge observations. Storm total rainfall for both observed and simulated fields show a large region of rainfall accumulations exceeding 100 mm extending up the East Coast, with maximum accumulations either along the track or left of the track. Time series of

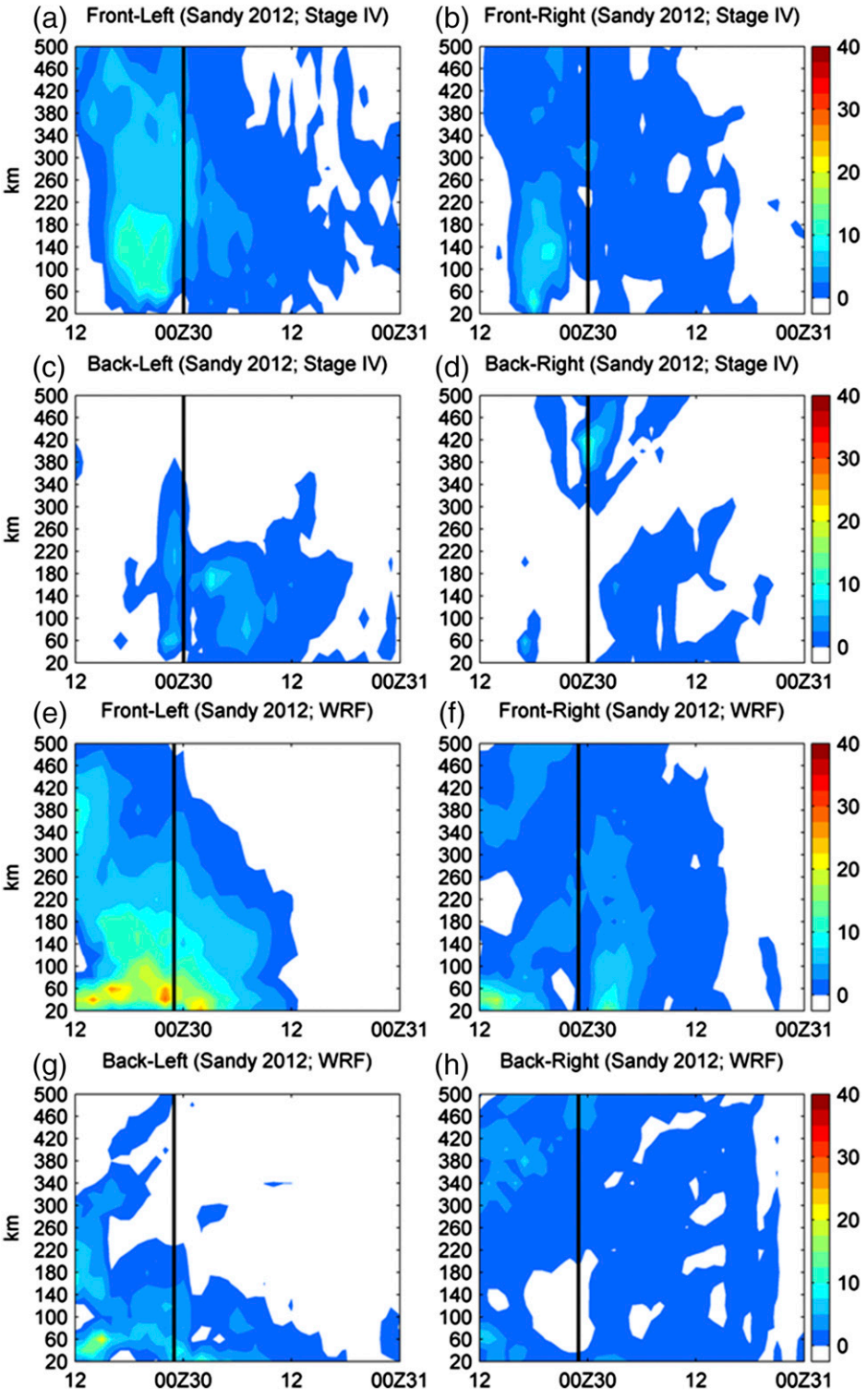

FIG. 21. As in Fig. 10, but for Hurricane Sandy. The black lines indicate the time of landfall, that is, 0000 UTC 30 Oct for best track and 2300 UTC 29 Oct for WRF run.

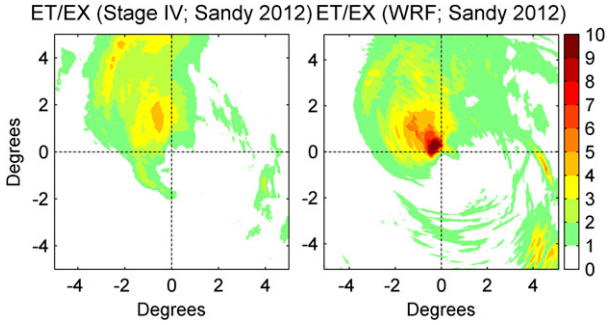

FIG. 22. The rainfall composite of stage IV and WRF simulation for Hurricane Sandy during ET/EX stage.

simulated mean rainfall (at rain gauge locations) closely match mean rainfall from rain gauges.

2) There are pronounced changes over time in the distribution of rainfall, relative to the center of circulation of the storm. Lagrangian analyses of rainfall structure and evolution show a concentration of rainfall in the left-front quadrant of Irene, both in observed rainfall fields and in the high-resolution simulations. Time series of mean rainfall for the inner rainband region of the storm (within 100 km of the center of circulation) show pronounced peaks in observed and simulated fields between 0900 and 1500 UTC 27 Aug, corresponding to the period around the first landfall. Although the time series of inner rainband rainfall match well, the spatial distribution of the landfall maxima in rainfall differ for observed and simulated rainfall fields. Throughout the life cycle of the storm, overestimation of rainfall is largely tied to the outer rainband region.
3) Extratropical transition of Hurricane Irene was characterized by a period of rapid transition from 1800 UTC 27 Aug to 2000 UTC 29 Aug, in which the thickness asymmetry increased from 0 to 50 m and the lower thermal wind rapidly decreased to 0 m s^{-1}, marking the transition to cold core structure in the lower atmosphere. The period of extratropical transition is also characterized by rapid increase in wind shear from 12 to 25 m s^{-1}. PV analyses highlight the interactions of Irene's circulation with an approaching trough that play a central role in extratropical transition. The composite rainfall distribution of Irene before extratropical transition showed a right-of-track rainfall pattern before ET and a left-of-track distribution after it moved into the ET period.
4) Mountainous terrain plays a critical role in determining the locations of extreme rainfall and flooding from Hurricane Irene, like many tropical cyclones that make landfall in the eastern United States. A numerical experiment was carried out with WRF in which mountainous terrain in the northeastern United States was removed. The rainfall difference between the control simulation and the nonterrain simulation show that orographic enhancement of rainfall can be as large as ~80 mm in the New England area. A simple 1D model produces comparable rainfall with WRF simulation in Vermont, highlighting the impact of upslope lifting mechanism on orographic rainfall.
5) Analyses of rainfall distribution from Hurricane Hanna show that tropical cyclones with similar tracks and with similar temporal evolution of ET, as reflected in the cyclone phase space asymmetry and lower thermal wind time series, can exhibit different evolution of rainfall structure over land. Hanna and Irene differ markedly in terms of convective intensity and spatial distribution of rainfall. Lightning in Hurricane Hanna was concentrated in the inner region of the storm, producing clusters of heavy rainfall close to the center of circulation. Convective intensity for Irene was greatest for outer rainbands in the right-front quadrant close to landfall.
6) The track of Hurricane Sandy was normal to the coastline, unlike Irene and Hanna, and rainfall and flooding were concentrated left-of-track in the mid-Atlantic region. Rainfall from Sandy was concentrated in the left-front quadrant of the storm, with much of the rainfall occurring around the time of landfall, even in the mountainous terrain of the central Appalachians. Both observed and simulated rainfall show rainfall maxima in the mountainous central Appalachians. Simulated rainfall has pronounced maxima on the windward slopes, while observed rainfall is more uniformly distributed through the central Appalachians.

Acknowledgments. This work was partially funded by the NOAA Cooperative Institute for Climate Sciences (Grant NNX13AG94G), the National Science Foundation (Grant EAR-1520683), and Award NA14OAR4830101 from the National Oceanic and Atmospheric Administration, U.S. Department of Commerce (recipient of this award is Gabriel Vecchi; not an author of this paper). NLDN data were provided by the NASA Lightning Imaging Sensor (LIS) instrument team and the LIS data center via the Global Hydrology Resource Center (GHRC) located at the Global Hydrology and Climate Center (GHCC), Huntsville, Alabama through a license agreement with Global Atmospherics, Inc.

(GAI). The data available from the GHRC are restricted to LIS science team collaborators and to NASA EOS and TRMM investigators. We thank Dr. Mary Lynn Baeck for helping process radar data.

REFERENCES

Akter, N., and K. Tsuboki, 2012: Numerical simulation of Cyclone Sidr using a cloud-resolving model: Characteristics and formation process of an outer rainband. *Mon. Wea. Rev.*, **140**, 789–810, doi:10.1175/2011MWR3643.1.

Ashley, S. T., and W. S. Ashley, 2008: Flood fatalities in the United States. *J. Appl. Meteor. Climatol.*, **47**, 805–818, doi:10.1175/2007JAMC1611.1.

Atallah, E. H., and L. F. Bosart, 2003: The extratropical transition and precipitation distribution of Hurricane Floyd (1999). *Mon. Wea. Rev.*, **131**, 1063–1081, doi:10.1175/1520-0493(2003)131<1063:TETAPD>2.0.CO;2.

——, ——, and A. R. Aiyyer, 2007: Precipitation distribution associated with landfalling tropical cyclones over the eastern United States. *Mon. Wea. Rev.*, **135**, 2185–2206, doi:10.1175/MWR3382.1.

Avila, L. A., and J. Cangialosi, 2011: Tropical cyclone report, Hurricane Irene, 21–28 August 2011. National Hurricane Center, 45 pp. [Available online at http://www.nhc.noaa.gov/data/tcr/AL092011_Irene.pdf.]

Bao, X., and Coauthors, 2015: Diagnostics for an extreme rain event near Shanghai during the landfall of Typhoon Fitow (2013). *Mon. Wea. Rev.*, **143**, 3377–3405, doi:10.1175/MWR-D-14-00241.1.

Barlow, M., 2011: Influence of hurricane-related activity on North American extreme precipitation. *Geophys. Res. Lett.*, **38**, L04705, doi:10.1029/2010GL046258.

Barthel, F., and E. Neumayer, 2012: A trend analysis of normalized insured damage from natural disasters. *Climatic Change*, **113**, 215–237, doi:10.1007/s10584-011-0331-2.

Blackwell, K. G., 2000: The Evolution of Hurricane Danny (1997) at landfall: Doppler-observed eyewall replacement, vortex contraction/intensification, and low-level wind maxima. *Mon. Wea. Rev.*, **128**, 4002–4016, doi:10.1175/1520-0493(2000)129<4002:TEOHDA>2.0.CO;2.

Blake, E. S., C. W. Landsea, and E. J. Gibney, 2011: The deadliest, costliest, and most intense United States tropical cyclones of from 1851 to 2010 (and other frequently requested hurricane facts). NOAA Tech. Memo. NWS NHC-6, 47 pp. [Available online at http://www.nhc.noaa.gov/pdf/nws-nhc-6.pdf.]

Bosart, L. F., and G. M. Lackmann, 1995: Postlandfall tropical cyclone reintensification in a weakly baroclinic environment: A case study of Hurricane David (September 1979). *Mon. Wea. Rev.*, **123**, 3268–3291, doi:10.1175/1520-0493(1995)123<3268:PTCRIA>2.0.CO;2.

Brun, J., and A. P. Barros, 2014: Mapping the role of tropical cyclones on the hydroclimate of the southeast United States: 2002–2011. *Int. J. Climatol.*, **34**, 494–517, doi:10.1002/joc.3703.

Chen, S. Y. S., J. A. Knaff, and F. D. Marks, 2006: Effects of vertical wind shear and storm motion on tropical cyclone rainfall asymmetries deduced from TRMM. *Mon. Wea. Rev.*, **134**, 3190–3208, doi:10.1175/MWR3245.1.

Colle, B. A., 2003: Numerical simulations of the extratropical transition of Floyd (1999): Structural evolution and responsible mechanisms for the heavy rainfall over the northeast United States. *Mon. Wea. Rev.*, **131**, 2905–2926, doi:10.1175/1520-0493(2003)131<2905:NSOTET>2.0.CO;2.

Corbosiero, K. L., and J. Molinari, 2002: The effects of vertical wind shear on the distribution of convection in tropical cyclones. *Mon. Wea. Rev.*, **130**, 2110–2123, doi:10.1175/1520-0493(2002)130<2110:TEOVWS>2.0.CO;2.

——, and ——, 2003: The relationship between storm motion, vertical wind shear, and convective asymmetries in tropical cyclones. *J. Atmos. Sci.*, **60**, 366–376, doi:10.1175/1520-0469(2003)060<0366:TRBSMV>2.0.CO;2.

Didlake, A. C., and R. A. Houze, 2009: Convective-scale downdrafts in the principal rainband of Hurricane Katrina (2005). *Mon. Wea. Rev.*, **137**, 3269–3293, doi:10.1175/2009MWR2827.1.

Dong, M., L. Chen, Y. Li, and C. Lu, 2010: Rainfall reinforcement associated with landfalling tropical cyclones. *J. Atmos. Sci.*, **67**, 3541–3558, doi:10.1175/2010JAS3268.1.

Evans, J. L., and R. E. Hart, 2003: Objective indicators of the life cycle evolution of extratropical transition for Atlantic tropical cyclones. *Mon. Wea. Rev.*, **131**, 909–925, doi:10.1175/1520-0493(2003)131<0909:OIOTLC>2.0.CO;2.

Gao, S., Z. Meng, F. Zhang, and L. F. Bosart, 2009: Observational analysis of heavy rainfall mechanisms associated with severe Tropical Storm Bilis (2006) after its landfall. *Mon. Wea. Rev.*, **137**, 1881–1897, doi:10.1175/2008MWR2669.1.

Griffin, K. S., and L. F. Bosart, 2014: The extratropical transition of Tropical Cyclone Edisoana (1990). *Mon. Wea. Rev.*, **142**, 2772–2793, doi:10.1175/MWR-D-13-00282.1.

Hart, R. E., 2003: A cyclone phase space derived from thermal wind and thermal asymmetry. *Mon. Wea. Rev.*, **131**, 585–616, doi:10.1175/1520-0493(2003)131<0585:ACPSDF>2.0.CO;2.

Hoskins, B. J., M. E. McIntyre, and A. W. Robertson, 1985: On the use and significance of isentropic potential vorticity maps. *Quart. J. Roy. Meteor. Soc.*, **111**, 877–946, doi:10.1002/qj.49711147002.

Huang, H.-L., M.-J. Yang, and C.-H. Sui, 2014: Water budget and precipitation efficiency of Typhoon Morakot (2009). *J. Atmos. Sci.*, **71**, 112–129, doi:10.1175/JAS-D-13-053.1.

Jones, S. C., and Coauthors, 2003: The extratropical transition of tropical cyclones: Forecast challenges, current understanding, and future directions. *Wea. Forecasting*, **18**, 1052–1092, doi:10.1175/1520-0434(2003)018<1052:TETOTC>2.0.CO;2.

Kitabatake, N., 2011: Climatology of extratropical transition of tropical cyclones in the western North Pacific defined by using cyclone phase space. *J. Meteor. Soc. Japan*, **89**, 309–325, doi:10.2151/jmsj.2011-402.

Knight, D. B., and R. E. Davis, 2009: Contribution of tropical cyclones to extreme rainfall events in the southeastern United States. *J. Geophys. Res.*, **114**, D23102, doi:10.1029/2009JD012511.

Konrad, C. E., and L. B. Perry, 2010: Relationships between tropical cyclones and heavy rainfall in the Carolina region of the USA. *Int. J. Climatol.*, **30**, 522–534, doi:10.1002/joc.1894.

Kunkel, K. E., D. R. Easterling, D. A. R. Kristovich, B. Gleason, L. Stoecker, and R. Smith, 2010: Recent increases in U.S. heavy precipitation associated with tropical cyclones. *Geophys. Res. Lett.*, **37**, L24706, doi:10.1029/2010GL045164.

Langousis, A., and D. Veneziano, 2009: Theoretical model of rainfall in tropical cyclones for the assessment of long-term risk. *J. Geophys. Res.*, **114**, D02106, doi:10.1029/2008JD010080.

Lin, N., J. A. Smith, G. Villarini, T. P. Marchok, and M. L. Baeck, 2010: Modeling extreme rainfall, winds, and surge from Hurricane Isabel (2003). *Wea. Forecasting*, **25**, 1342–1361, doi:10.1175/2010WAF2222349.1.

Lin, Y., and K. E. Mitchell, 2005: The NCEP stage II/IV hourly precipitation analyses: Development and applications. *19th*

Conf. on Hydrology, San Diego, CA, Amer. Meteor. Soc., 1.2. [Available online at https://ams.confex.com/ams/Annual2005/webprogram/Paper83847.html.]

Lonfat, M., R. Rogers, T. Marchok, and F. D. Marks Jr., 2007: A parametric model for predicting hurricane rainfall. *Mon. Wea. Rev.*, **135**, 3086–3097, doi:10.1175/MWR3433.1.

Marchok, T., R. Rogers, and R. Tuleya, 2007: Validation schemes for tropical cyclone quantitative precipitation forecasts: Evaluation of operational models for U.S. landfalling cases. *Wea. Forecasting*, **22**, 726–746, doi:10.1175/WAF1024.1.

Marks, F. D., G. Kappler, and M. DeMaria, 2002: Development of a tropical cyclone Rainfall Climatology and Persistence (RCLIPER) model. Preprints, *25th Conf. on Hurricanes and Tropical Meteorology*, San Diego, CA, Amer. Meteor. Soc., 327–328.

Milrad, S. M., E. H. Atallah, and J. R. Gyakum, 2009: Dynamical and precipitation structures of poleward-moving tropical cyclones in eastern Canada, 1979–2005. *Mon. Wea. Rev.*, **137**, 836–851, doi:10.1175/2008MWR2578.1.

Moon, Y., and D. S. Nolan, 2015: Spiral rainbands in a numerical simulation of Hurricane Bill (2009). Part I: Structures and comparisons to observations. *J. Atmos. Sci.*, **72**, 164–190, doi:10.1175/JAS-D-14-0058.1.

Orville, R. E., and G. R. Huffines, 2001: Cloud-to-ground lightning in the United States: NLDN results in the first decade, 1989–98. *Mon. Wea. Rev.*, **129**, 1179–1193, doi:10.1175/1520-0493(2001)129<1179:CTGLIT>2.0.CO;2.

Rogers, R., S. Chen, J. Tenerelli, and H. Willoughby, 2003: A numerical study of the impact of vertical shear on the distribution of rainfall in Hurricane Bonnie (1998). *Mon. Wea. Rev.*, **131**, 1577–1599, doi:10.1175//2546.1.

Smith, J. A., G. Villarini, and M. L. Baeck, 2011: Mixture distributions and the hydroclimatology of extreme rainfall and flooding in the eastern United States. *J. Hydrometeor.*, **12**, 294–309, doi:10.1175/2010JHM1242.1.

Smith, R. B., 1979: The influence of mountains on the atmosphere. *Advances in Geophysics*, Vol. 21, Academic Press, 87–230, doi:10.1016/S0065-2687(08)60262-9.

——, P. Schafer, D. Kirshbaum, and E. Regina, 2009: Orographic enhancement of precipitation inside Hurricane Dean. *J. Hydrometeor.*, **10**, 820–831, doi:10.1175/2008JHM1057.1.

Song, J. J., J. J. Han, and Y. A. Wang, 2011: Cyclone phase space characteristics of the extratropical transitioning tropical cyclones over the western North Pacific. *Acta Meteor. Sin.*, **25**, 78–90, doi:10.1007/s13351-011-0006-y.

Sturdevant-Rees, P., J. A. Smith, J. Morrison, and M. L. Baeck, 2001: Tropical storms and the flood hydrology of the central Appalachians. *Water Resour. Res.*, **37**, 2143–2168, doi:10.1029/2000WR900310.

Sun, X., and A. P. Barros, 2012: The impact of forcing datasets on the high-resolution simulation of Tropical Storm Ivan (2004) in the southern Appalachians. *Mon. Wea. Rev.*, **140**, 3300–3326, doi:10.1175/MWR-D-11-00345.1.

Tuleya, R. E., M. DeMaria, and R. J. Kuligowski, 2007: Evaluation of GFDL and simple statistical model rainfall forecasts for U.S. landfalling tropical storms. *Wea. Forecasting*, **22**, 56–70, doi:10.1175/WAF972.1.

Villarini, G., and J. A. Smith, 2010: Flood peak distributions for the eastern United States. *Water Resour. Res.*, **46**, W06504, doi:10.1029/2009WR008395.

——, and ——, 2013: Spatial and temporal variability of cloud-to-ground lightning over the continental U.S. during the period 1995–2010. *Atmos. Res.*, **124**, 137–148, doi:10.1016/j.atmosres.2012.12.017.

——, ——, M. L. Baeck, T. Marchok, and G. A. Vecchi, 2011: Characterization of rainfall distribution and flooding associated with U.S. landfalling tropical cyclones: Analyses of Hurricanes Frances, Ivan, and Jeanne (2004). *J. Geophys. Res.*, **116**, D23116, doi:10.1029/2011JD016175.

——, R. Goska, J. A. Smith, and G. A. Vecchi, 2014: North Atlantic tropical cyclones and U.S. flooding. *Bull. Amer. Meteor. Soc.*, **95**, 1381–1388, doi:10.1175/BAMS-D-13-00060.1.

Wang, Q., Q. Li, and G. Fu, 2012: Determining the extratropical transition onset and completion times of Typhoons Mindulle (2004) and Yagi (2006) using four methods. *Wea. Forecasting*, **27**, 1394–1412, doi:10.1175/WAF-D-11-00148.1.

Wood, K. M., and E. A. Ritchie, 2014: A 40-year climatology of extratropical transition in the eastern North Pacific. *J. Climate*, **27**, 5999–6015, doi:10.1175/JCLI-D-13-00645.1.

Xie, B., and F. Zhang, 2012: Impacts of typhoon track and island topography on the heavy rainfalls in Taiwan associated with Morakot (2009). *Mon. Wea. Rev.*, **140**, 3379–3394, doi:10.1175/MWR-D-11-00240.1.

Yu, C.-K., and L.-W. Cheng, 2013: Distribution and mechanisms of orographic precipitation associated with Typhoon Morakot (2009). *J. Atmos. Sci.*, **70**, 2894–2915, doi:10.1175/JAS-D-12-0340.1.